Air Force Institute of Technology
AFIT Scholar

Theses and Dissertations | Student Graduate Works

3-23-2017

The Fresnel Zone Light Field Spectral Imager

Francis D. Hallada

Follow this and additional works at: https://scholar.afit.edu/etd

 Part of the Optics Commons

Recommended Citation
Hallada, Francis D., "The Fresnel Zone Light Field Spectral Imager" (2017). *Theses and Dissertations*. 786.
https://scholar.afit.edu/etd/786

This Thesis is brought to you for free and open access by the Student Graduate Works at AFIT Scholar. It has been accepted for inclusion in Theses and Dissertations by an authorized administrator of AFIT Scholar. For more information, please contact richard.mansfield@afit.edu.

The Fresnel Zone Light Field Spectral Imager

THESIS

Francis D. Hallada, Maj, USAF

AFIT-ENP-MS-17-M-095

DEPARTMENT OF THE AIR FORCE
AIR UNIVERSITY

AIR FORCE INSTITUTE OF TECHNOLOGY

Wright-Patterson Air Force Base, Ohio

DISTRIBUTION STATEMENT A
APPROVED FOR PUBLIC RELEASE; DISTRIBUTION UNLIMITED

The views expressed in this document are those of the author and do not reflect the official policy or position of the United States Air Force, the United States Department of Defense or the United States Government. This material is declared a work of the U.S. Government and is not subject to copyright protection in the United States.

AFIT-ENP-MS-17-M-095

THE FRESNEL ZONE LIGHT FIELD SPECTRAL IMAGER

THESIS

Presented to the Faculty

Department of Engineering Physics

Graduate School of Engineering and Management

Air Force Institute of Technology

Air University

Air Education and Training Command

in Partial Fulfillment of the Requirements for the

Degree of Master of Science

Francis D. Hallada, BS

Maj, USAF

Mar 2017

DISTRIBUTION STATEMENT A
APPROVED FOR PUBLIC RELEASE; DISTRIBUTION UNLIMITED

AFIT-ENP-MS-17-M-095

THE FRESNEL ZONE LIGHT FIELD SPECTRAL IMAGER

THESIS

Francis D. Hallada, BS
Maj, USAF

Committee Membership:

Lt. Col. Anthony L. Franz, PhD
Chair

Dr. Michael R. Hawks
Member

Dr. Michael A. Marciniak
Member

Abstract

This thesis provides a computational model and the first experimental demonstration of a Fresnel zone light field spectral imaging (FZLFSI) system. This type of system couples an axial dispersion binary diffractive optic with light field (plenoptic) camera designs providing a snapshot spectral imaging capability. A computational model of the system was developed based on wave optics methods using Fresnel propagation. It was validated experimentally and provides excellent demonstration of system capabilities. The experimentally demonstrated system was able to synthetically refocus monochromatic images across greater than a 100nm bandwidth. Furthermore, the demonstrated system was modeled to have a full range of approximately 400 to 800nm with close to a 15nm spectral sampling interval. While images of multiple diffraction orders were observed in the measured light fields, they did not degrade the system's performance. Experimental demonstration also showed the capability to resolve between and process two different spectral signatures from a single snapshot. For future FZLFSI designs, the study noted there is a fundamental design trade-off, where improved spectral and spatial resolution reduces the spectral range of the system.

Dedicated to my loving wife

Acknowledgements

First and foremost, I'd like to thank the members of the 88th Test and Evaluation squadron who saved my life on 1 June 2014, exemplifying the rescue motto, "That others may live." Then, the medical care provided by the University Medical Center of Southern Nevada Trauma and Burn Center set a firm foundation for my recovery while preserving mine and my family's dignity. Additionally, the countless professionals from Healthsouth and the Nevada Community Enrichment Program helped guide me to the right path for continued recovery. I thank all these people for their hard work and dedication that made the goal of pursuing this degree become a reality.

I'm thankful for my wonderful wife who has been a rock throughout this interesting journey. She has stood by me day and night as I studied and worked on this project. Always helping me to retain a healthy balance in my life between work and family. Her support has enabled all the time and effort I've spent on this project. I'd also like to thank my father who helped me retain the right perspective throughout this project. He was instrumental in shaping this thesis through all the time he spent providing comments on my early drafts of the paper.

Finally, I'd like to thank my committee who helped me present a thorough analysis of the study. My research advisor, Lt Col Franz, helped me to maintain momentum throughout this work, especially at times when I was uncertain about what was "the next step."

Francis D. Hallada

Table of Contents

List of Figures

List of Tables

THE FRESNEL ZONE LIGHT FIELD SPECTRAL IMAGER

I. Introduction

The Fresnel zone plate (FZP) is a diffractive optic with the resolving power of a lens of the same diameter [1]. Traditionally, one distinct advantage of the FZP over refractive optics is it can be used for imaging in spectral regions, such as extreme ultraviolet and soft x-rays, where solids are highly absorbing [2]. On the other hand, a typically undesirable aspect of the FZP is that focal length varies greatly with wavelength, making axial chromatic aberration (ACA) quite severe [3]. Figure 1 demonstrates the ACA of a binary diffractive optic based on FZP theory, the photon sieve, with a half meter focal length. As a result, much of the previous research involving imaging with binary diffractive optics of this sort has considered methods for reducing this aberration in order to image targets over reasonable spectral bandwidths [4, 5]. Conversely, it has been demonstrated that the ACA of diffractive optics might be exploited for high resolution spectral imaging by physical translation of the sensor array along the optic axis to measure different image formation planes [6, 7]. As a dispersive spectrometer, the concept of the system is similar to that of a linear grating. Instead of lateral dispersion of the spectra, now

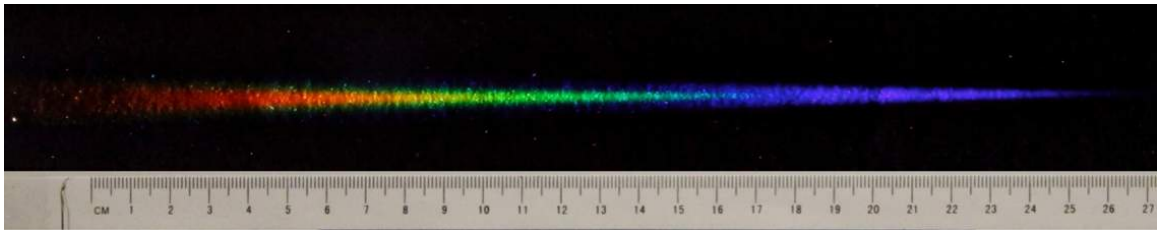

Figure 1. The ACA of FZP-type optics was demonstrated using a 500mm focal length photon sieve illuminated by a white light LED. This picture was set-up and taken with the help of Will Dickinson.

the dispersion is axial.

This thesis investigates computational spectral imaging using binary optics based on FZP theory coupled with a light field detection assembly. The different image formation planes for each wavelength are constructed synthetically through processing the collected light field. This concept has been recently proposed as a potential design for a spectral imager, which collects the spatial and spectral dimensions in a single exposure [8].

A light field detector samples both the position and angle of rays within the camera. In contrast, the detector array in a conventional camera measures the radiance integrated over all directions of rays incident upon each sensor pixel. Sampling both position and angle adds a significant new quality to the recorded data. Previous research on light field cameras has focused on methods to process this new richness of data from the imaged scene, specifically, constructing digitally refocused, synthetic photographs and estimation of specific object depths within a scene [9, 10, 11]. Additionally, light field imaging has shown great promise for microscopy applications like volumetric imaging of weakly scattering samples [12]. Light field microscopy (LFM) research has shown that 3-d deconvolution methods can be used to reconstruct good estimates for the voxels of a 3-d sample.

In this study, the objective optic of the light field camera is a FZP, imaging a distant scene, so digital refocusing and 3-d deconvolution methods now provide a way to interrogate the spectral structure of the collected signal. This thesis seeks to demonstrate and provide basic characterization of a Fresnel zone light field spectral imager (FZLFSI). The FZLSI will computationally generate a 3-d spectral data cube from a snapshot collection of the light field produced by optics based on Fresnel zone theory.

1.1 Motivation

The full potential of diffractive optics based on FZP theory has been continuously explored since they were first demonstrated by Lord Rayleigh. Now coupled with the light field camera concepts, new opportunities emerge to capitalize on the unique character of these optics. The focal spot size of a FZP is related to the diameter of the optic similar as is found with refractive lenses. However, the precision of current fabrication methods limits the maximum achievable diameter. Essentially, a FZP is constructed from a series of concentric annular regions of decreasing width. The outermost rings define the resolution limit to accurately print the zone plate structure. Currently, electron beam lithography techniques have been demonstrated to define structures smaller than 10nm [13]. However, this remains a fundamental limitation on production of FZP optics. This fabrication constraint for optics based on Fresnel zone theory has been addressed in previous work through the development of zone plates with modified structures [14] and the photon sieve [15].

The photon sieve is composed of pinhole apertures of varying diameters aligned with the Fresnel half-period zones that will be described in Sec. 2.1. These apertures can be fabricated with widths greater than the underlying zone, allowing fabrication of larger diameter optics than traditional FZP designs. Furthermore, the distribution of these apertures can be controlled in such a way as to suppress higher orders of diffraction [15]. For optical wavelengths, photon sieves have been demonstrated with diameters of 0.1m for a 1m focal length while maintaining diffraction limited focusing [16]. The possibility exists to fabricate and deploy photon sieve optics with much larger diameters. The photon sieve offers significant potential for small satellite sensor payloads as demonstrated by a payload designed and tested for USAFA's FalconSAT-7 [17]. However, this type of optic is restricted to operation within a narrow bandwidth because of severe chromatic aberration.

The imaging concept developed in this paper uses this dispersive power to measure the spectral structure of a scene, and furthermore, could be used for panchromatic imaging with photon sieves over broader bandwidths.

The axial dispersion of FZP-type optics enables a simple extension of light field camera concepts and allows computation of the spectral structure of an image collected in a single exposure. The concepts of synthetic photography and 3-d light field deconvolution are well demonstrated in previous studies, and these same processing algorithms can be simply modified to instead generate spectral data cubes. However, measuring this added dimension of the scene comes at a price. In order to capture the angular dimensionality of rays within the camera, some spatial resolution must be sacrificed as will be described in Section 2.2. The camera in this paper maximizes angular sampling since it is based on the earlier plenoptic camera designs, but the presented concepts will apply to generalized light field camera designs. Other light field camera designs have been demonstrated which offer much better spatial resolution while preserving much of the angular sampling characteristics by modifying the micro-lens array and detector placement [10, 18]. The design trade-offs for the light field detector assembly in the FZLFSI need to be better understood so future systems can be designed to meet specific operational requirements. This paper provides the starting point from which different light field camera designs may be investigated for more refined application of this spectral imaging concept.

1.2 Objectives

The goal of this project is to demonstrate a FZLFSI design and analyze its performance in order to better understand the capabilities this new type of detector provides. Part of achieving this target requires identifying the specific relationships

between the optical design parameters and resolution, both spatial and spectral. The spectral resolution of the FZP depends on the total number of transparent zones [19], similar in concept to the resolving power of a linear grating. Incorporating the FZP into a light field camera design adds new complication because it modifies the precision of how the spatial and spectral dimensions are sampled. There is an inherent trade-off in light field cameras between spatial and angular sampling [20, 21]. The complicated relationships between the FZP and light field camera optical designs must be explored to better understand how to optimize the FZLFSI for particular applications.

The FZLFSI will be demonstrated in this thesis through computer simulation and experimental verification. Digital spectral refocusing will be demonstrated as well as computation of the spectral structure of isolated pixels. The scope of this project is limited to basic performance of the system and will not directly evaluate the merits of a FZP and its use as an imaging optic. Additionally, only imaging at optical infinity is considered to avoid the challenges of deconvolution based on both object distance and wavelength. Spectral profiles will only be computed for isolated pixels and a full 3-d light field deconvolution method will not be presented. The objective of this project is to demonstrate the concept, providing fundamental characterization and setting the stage for further development. This thesis advances research in this area by providing experimental verification of the FZLFSI concept and a computation model for evaluating the performance of future system designs.

II. Background and Theory

The FZLFSI is most easily described by separately introducing the theory behind the two major components, FZP optics and the light field camera. The first section describes general FZP theory with an emphasis on the focusing effects of the FZP and its axial dispersion properties. Next, the light field camera is introduced concentrating primarily on basic synthetic photography concepts. The discussion in this thesis is limited to the traditional plenoptic camera which is a type of light field camera where the micro-lens array is fixed at the focal plane of the objective optic.

2.1 Fresnel Zone Plate

Fresnel diffraction theory establishes the fundamental principles on which the FZP is based. Consider a planar wavefront and an observation point normal to the wave front at distance r_0. The Huygens-Fresnel principle states, every point along the wavefront can be represented as a secondary emitting point source. The resulting wavefront at any later instant can then be constructed from the superposition of the wavelets from the secondary emitters, with obliquity taken into account [22, p. 444]. Fresnel half-period zones are then represented by constructing a series of concentric spheres centered at the observation point, starting at radius r_0 and increasing by a half wavelength each time. These spheres represent discrete values of the optical path length (OPL) from the observation point. The annular regions defined by where the spheres intersect the wavefront are called Fresnel half-period zones as illustrated in Fig. 2. The optical path difference (OPD) between all wavelets from a single zone arriving at the observation point remains within a half wavelength. Therefore, the wavelets from a single zone serve to reinforce each other. However, for each wavelet from a particular zone there is a

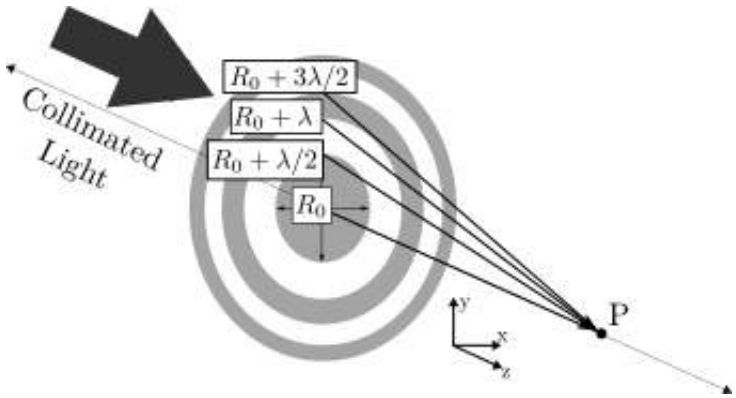

Figure 2. The Fresnel half-period zones are defined by the regions of a planar wavefront with less than a half-wavelength OPD to observation point P. R_0 is the OPL orthogonal to the wavefront.

wavelet generated in the successive zone with a π difference in phase. Thus, adjacent zones will tend to cancel each other out. As a result, the net contribution at the observation point from all the unobstructed zones is approximately equal to half the contribution from the first zone. If every other half-period zone is obstructed, the net effect will be significant constructive interference at the observation point from the diffracted wavelets. This is how a FZP achieves focus [22, p. 495]. The following discussion of Fresnel zone theory presents general characteristics that are common to all diffractive optics based on the same principles, like photon sieves and kinoform lenses. The equations that will be presented also accurately describe the character of these optics. This study only considered the FZP, but consistent results would be expected from similar diffrative optics.

The basic FZP structure is composed of an array of concentric, transparent rings. The radii of the rings are calculated by considering the OPD between an axial ray and a ray passing through the n^{th} transparent zone. Referring to Fig. 3, the Pythagorean theorem is used to express an OPD between successive zones that is an integral number of wavelengths. This relation solved for r_n, the radius to the center of the nth, transparent zone becomes

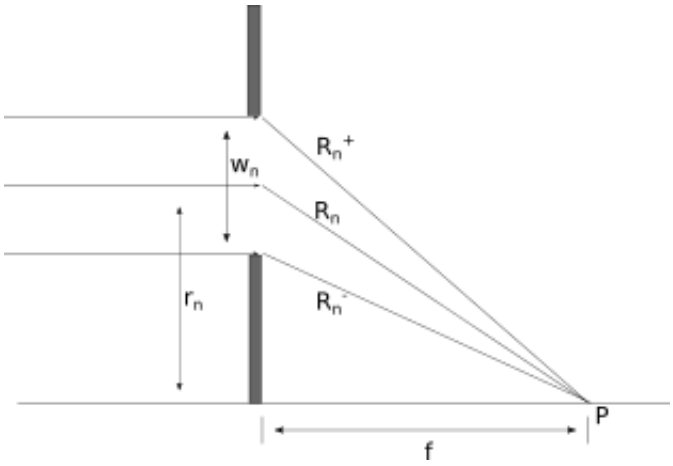

Figure 3. The geometry of the FZP structure that ensures the OPD to point P for the marginal rays in each zone, R_n^+ and R_n^- , remain within a half wavelength. The zone structure can be described by the radius to the center of the nth zone, r_n, and the width of the zone, w_n, using the equations from the text.

$$r_n^2 = 2nf_0\lambda_0 + n^2\lambda_0^2. \tag{1}$$

Where f_0 and λ_0 indicate the design focal length and wavelength for the FZP. For most cases $\lambda_0/f_0 \ll 1$, so the second term in the above expression can be neglected [23, p. 375]. With this approximation, the design focal length is

$$f_0 \approx \frac{r_n^2}{2n\lambda_0}. \tag{2}$$

Wavelengths other than the design wavelength will also be focused by similar diffraction geometry. The focal lengths for these wavelengths are calculated by recognizing that the term $r_n^2/2n$ is a constant parameter for a particular zone plate [1], and other wavelengths still must satisfy Eq. 1. Therefore, the relationship can be expressed as

$$f_\lambda = \frac{f_0\lambda_0}{\lambda} \tag{3}$$

where f_λ is the focal length for light with wavelength λ.

For negative zone plates, where the center zone is opaque, the inner radius of the first transparent zone sets the relative phase of the waves at the focus as compared to the unobstructed incident wavefront. The spacing between transparent zones then achieves the focusing effect, which is why Eq. 1 can be used to describe the center of each transparent zone. Also, it can be shown that the width of each zone is

$$w_n = \frac{\lambda_0 f_0}{2r_n} \tag{4}$$

[16]. This relation is derived from considering the OPD between R_+ and R_- then solving for the difference between the radii using a binomial expansion as is shown explicitly in [24].

For a FZP designed with the parameters discussed above, much research has been done on its focusing performance. Early on, it was shown that the diffraction pattern of the FZP approaches an Airy disk as the number of transparent zones increases [1, 25]. Additionally, the focusing performance of the zone plate remains sufficient for off-axis points. Considering a planar wavefront now incident on the FZP at an angle, the focus remains sharp for small angles [26]. Myers derived the following relation for the maximum angle, ϵ, to maintain good focus [1].

$$\left| \pm \left(2 f_0 n_{\max} \lambda\right)^{1/2} \left(\frac{n_{\max}\lambda}{f_0}\right) \sin\epsilon - n_{\max}\lambda \sin^2\epsilon \right| < \frac{1}{4}\lambda \tag{5}$$

This equation defines the maximum field of view (FOV) for this device. Beyond this angle, the error in the OPD from consecutive transparent rings will no longer produce well defined edges. For the FZPs in this paper, this condition is satisfied for close to a 6^o FOV.

With a spatial resolving power very close to a refractive lens, the unique aspect of the FZP exploited in this thesis is its axial dispersion. As shown by Eq. 3,

different wavelengths will be focused to different image formation planes. Sussman derives an expression for the axial irradiance at a given wavelength by integrating the fields transmitted by each annular ring and simplifying the result using a geometric series expansion [26]. The equation, with variable designations modified to fit the conventions in this thesis is

$$E\left(0,0,z\right)=\frac{K[1-\cos(2n_{\max}\pi f_{\lambda}/z)]}{(\pi f_{\lambda}/z)^{2}[1+\cos(\pi f_{\lambda}/z)]}, \tag{6}$$

for values of z not much larger than the first-order focal length, where K is a constant value for a particular zone plate design and $n_{\max}$ represents the number of open rings. The expression is important to this thesis because it models the spectral response of the FZP. The spectral line shape predicted by Eq. 6 can then be used to estimate the maximum spectral resolution expected for the FZP as shown in Fig. 4. Eq. 6 can also be thought of as describing the spectral depth of focus for the FZP. A narrow line shape means that spectral defocus occurs rapidly. Modeling different FZP designs using Eq. 6 shows that the spectral depth of focus is sharper for low f/# FZP designs. For spectral imaging with this type of optic, it is desirable that

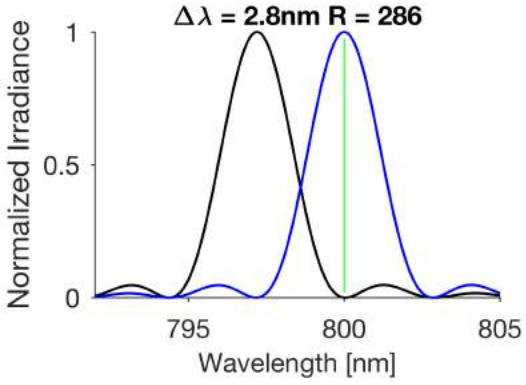

Figure 4. The spectral resolution of a FZP determined based on the Rayleigh criterion calculated using Eq. 6 in the text. This shows a resolving power of 286 for a zone plate designed for 800nm light with a focal length of 500mm and a diameter of approximately 30mm.

defocus due to wavelength occurs rapidly to limit spectral cross-talk between pixels [7].

Another interesting effect demonstrated from modeling the spectral irradiance close to the FZP using Eq. 6 is that there is more than a single maximum along the optical axis. In addition to the primary focal point, there are other points where relative maxima are observed. These other foci arise from the contributions of higher diffraction orders. They occur, with reduced irradiance, on the image side of the optic at distances of $\frac{1}{m}f$, for odd integer values of m. The appearance of these higher order focal points presents a limit on the spectral range for a detector that uses a standard FZP design. On the other hand, more modern FZP-type optics, photon sieves for example, can be constructed to suppress these higher order modes. The higher order modes arise because the rings in a standard FZP are symmetric, and the higher-order diffraction components from different sets of rings constructively interfere. This symmetry can be disrupted by random placement of the photon sieve's pinhole apertures across the underlying Fresnel zones [15]. Thus, photon sieves would not necessarily experience this spectral range limitation.

There has been some discussion of using a FZP as a miniaturized spectrometer [19]. This is being developed for applications such as hyperspectral microscopy. A key advantage of the FZP for these applications is that Fresnel diffraction remains appropriate for small optical distances as opposed to the Fraunhofer diffraction limits of typical linear gratings. The spectral resolution of the FZP does not depend on size but instead on the number of transparent zones, which offers a distinct advantage for miniaturization of a spectrometer [19]. This characteristic can also be seen in Eq. 6 where the sharpness of the peak only depends on the number of zones and the focal length. The FZP can provide excellent spectral resolution once the challenges in measuring axial dispersion are addressed.

A different study considered using a photon sieve for high resolution spectral imaging [6]. In this proposed system, the detector array is moved along the optical axis to physically conduct measurements at different image formation planes. This method highlights an important aspect of spectral imaging of this sort. Each imaging plane contains superimposed blurred and focused images from closely spaced spectral features. As mentioned earlier, a low f/# photon sieve is desirable to narrow the spectral depth of focus and limit this effect. Spectral imaging with a FZP-type optic presents a 3-d deconvolution problem due to the spatial and spectral dimensions. Solutions to this deconvolution problem have been shown to be well estimated through various computational methods, and as a result, photon sieve spectral imaging is possible with higher resolutions than other commonly used spectral imagers [6].

2.2 Light Field Camera

As the primary optic, the FZP sets the limit for the maximum achievable resolutions, spatial and spectral. However, the computational sampling precision of the spatial and spectral dimensions is determined by the optical design of the light field detector assembly. This section introduces light field camera theory to cultivate a better understanding of how this system can approach the limits set by the FZP. Conventional cameras do not record much about the structure of the light forming an image at the sensor array. Each pixel in the camera responds to the radiance of incident rays integrated over all angles collected by the primary optic. The term light field refers to the 4-d structure of the rays within the camera, both position and angle. The plenoptic camera was introduced in 1992 by Adelson and Wang as a device to measure the structure of the light field within the camera [20]. It is much like a conventional camera, however the sensor array is replaced by a micro-lens

array (MLA). Conceptually, the system can be represented as an array of small cameras which image the objective optic. Each micro-lens allows the rays for a single point at what was the conventional camera's image plane to be separately recorded based on incident angle at the micro-lens, as shown in Fig. 5. In the figure, a single point on the detector plane corresponds to a single direction of ray at a particular x value in the micro-lens plane. A single micro-lens collects all angles of rays within the camera for a distinct image point [27]. Therefore, the spatial sampling of the light field is set by the size of the micro-lenses and angular sampling is determined by the size of detector pixels.

Keeping track of and describing the light field within the camera is often a daunting task, so there are some conventions from within the light field community that will now be introduced. The light field can be conveniently expressed by correlating each ray with the point it intersects the primary optic (u, v) and its intersection with the micro-lens array (x, y). Using this notation, each micro-lens collects rays for a small range of x and y values across the full range of u and v. Then, each pixel in the image under the micro-lens relates to a small range of u and v. In this way, the light field can be expressed as a 4-d quantity $L(u, v, x, y)$ where (u, v) are the angular dimensions and (x, y) the positional dimensions. For simplicity, the light field will often be described geometrically in 2-d (u, x). Figure 6 is a first-order ray diagram for several distant, focused objects across a span of lateral positions. The figure shows the rays collected by each micro-lens and presents the basic construct for the light field within the camera. Part c) of the figure shows a different way to represent each ray based off the x and u values. In this ray-space plot, each point describes a single ray within the camera. The grid represents how these rays are sampled by the detector array. Each cell of the grid represents a single detector pixel. In this representation, it is easier to understand

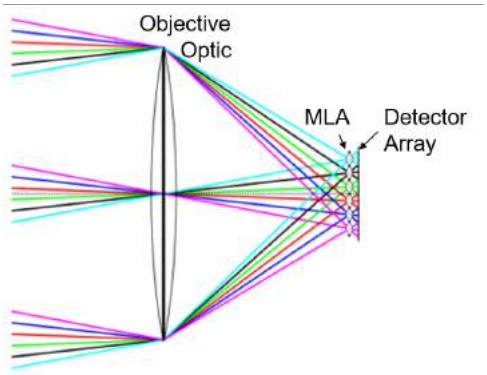

Figure 5. Each colored set designates three rays at the same incident angle from an object at infinity. These rays are then focused by the primary optic to a singe micro-lens. The rays propagate through the micro-lenses and are separated by incident angle. Each point on the detector corresponds to a distinct ray angle from the objective optic for a particular image point. The MLA is fixed at the back focal plane of the objective optic.

how micro-lens and detector sizes define spatial and angular sampling rates, respectively. As a result, this method is often more intuitive for understanding certain aspects of the light field and will be used again later in the paper.

Another useful convention for analyzing light fields involves two types of images that would be formed through considering the different light field dimensions. The first is the physical image formed under each micro-lens, which will be referred to as the micro-lens image. Using the 4-d light field variable designations introduced above, this image is constructed by the (u, v) elements for a particular value of x and y. In the ray-space plot of Fig. 6, this corresponds to a vertical rectangle with the width defined by the micro-lens apertures. This image is useful for evaluating the angular sampling of each image point at the micro-lens array. The second image construct commonly used is called the sub-aperture image. This term refers to the image that would be formed if there were pinhole apertures at specific locations spread across the objective optic [11]. These images are formed by the (x, y) elements of the light field at a particular (u, v) coordinate. In the ray-space diagrams, this is represented by a horizontal rectangle enclosing a small range of u

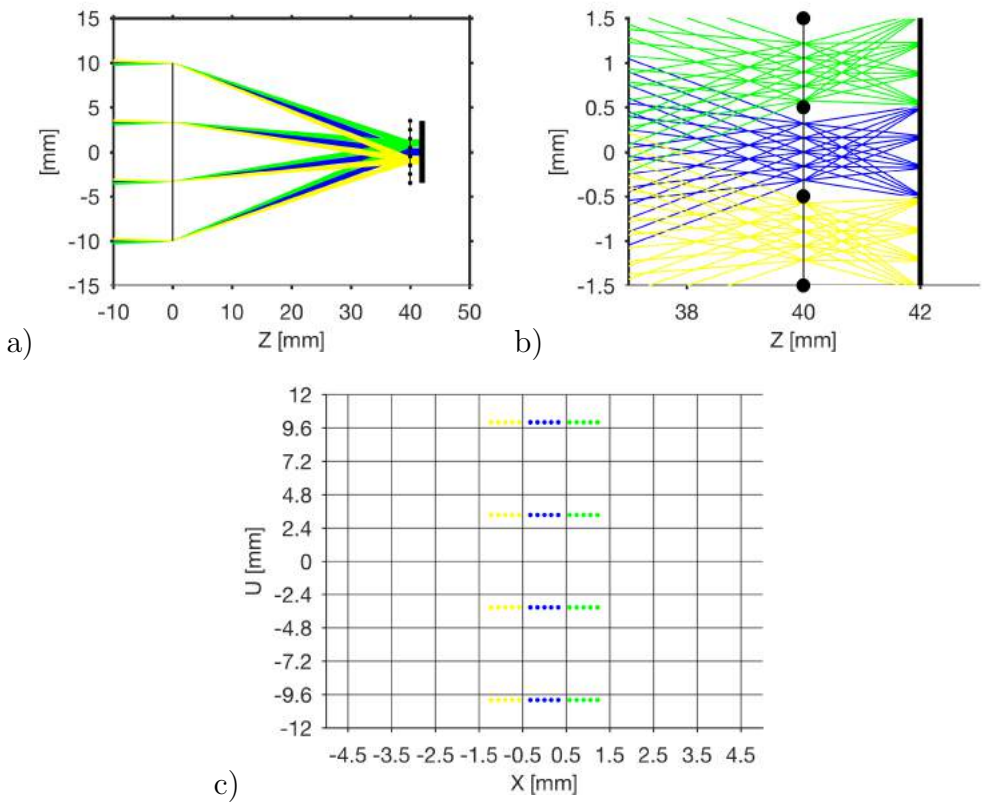

Figure 6. Rays from several distant objects with small lateral separations are traced through a traditional plenoptic camera. Four rays from each object point are traced through the system. The rays are color coded by micro-lens image. a) shows a geometric view of the light field camera system, b) is a magnified view of the micro-lens and detector planes. c) shows the same rays projected into ray-space coordinates defined by the location the ray intersects the objective, U, and position at the MLA, X. This ray-space diagram concept is adapted from ref. [11]. Each micro-lens image is formed by contributions from the rays across the entire objective optic aperture and are indicated by columns of the ray space plot. The grouping of rays that would create an image from a pinhole "sub-aperture" at a particular location on the objective optic are indicated by rows of the ray-space plot. Each cell of the grid in the ray-space plot indicates a detector pixel. See the text for additional description of these concepts.

values set by the size of the detector pixels. Each sub-aperture image shows the full scene with shifted parallax. The resolution of these images is the same as the final rendered image when standard digital refocusing algorithms are used. From these two descriptions of the images collected by the light field, it becomes clear that there is fundamentally a trade-off between spatial and angular resolution for a light field camera. The number of pixels within each micro-lens image sets the number of

different viewpoints, sub-aperture images, that can be constructed. In turn, if n x n pixels are dedicated to each micro-lens image, then the total achievable spatial resolution is reduced by the same factor when compared to a conventional camera system [20]. A graphical representation of how the light field dimensions and images are defined is presented in Fig. 7.

The micro-lens images define the angular sampling of the camera, and it is relevant to include a brief description of the design consideration that arises. In order to maximize the angular resolution, the image formed by the micro-lens should be as sharp as possible with substantial coverage of the detector array [10]. For sharp images, the micro-lenses need to be focused on the objective optic. Since the micro-lenses are small, the primary optic is essentially at optical infinity from their perspective. Therefore, the detector array is fixed at the micro-lens focal length to maintain good focus. In order to ensure this sharp focus, the separation must be accurate within

$$\Delta u \, (f_\mu / \Delta x) \tag{7}$$

where Δu is the width of a sensor pixel, Δx is the diameter of a micro-lens, and f_μ is the micro-lens focal length [10]. Next, in order to maximize coverage of the sensor array, the image side f/# of the primary optic and micro-lenses are matched. If the objective optic has a higher f/#, then there will be wasted sensor pixels between adjacent micro-lens images. If the f/# is lower, then there will be image overlap. Figure 2 in the Stanford Technical Report on plenoptic cameras has excellent pictures demonstrating this effect [10].

The angular sampling is what sets the plenoptic camera apart and fundamentally enables the computation of synthetic photographs. Synthetic photographs are computed through modifying how the detector pixels are integrated across the micro-lens images to render the final image. There are many ways the

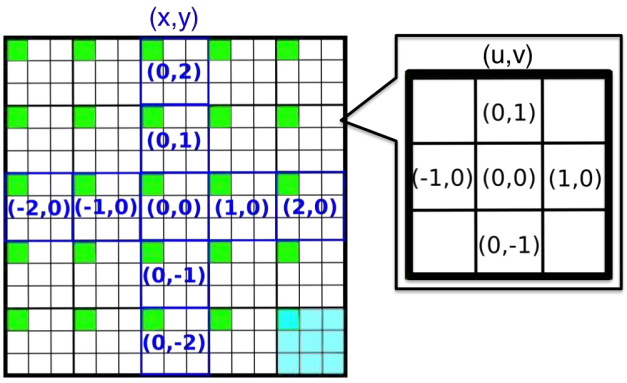

Figure 7. The 4 dimensions of the light field measured at the detector are defined as shown above. Each cell of the diagram represents a single detector pixel. The (x,y) dimensions depend on the position of the micro-lens image, and the (u,v) dimensions describe the pixel location within the micro-lens image. The numbering convention used in this thesis for the different dimensions is shown above. The origin for the (x,y) and (u,v) coordinates is the center micro-lens image and the center pixel in a particular image, respectively. The cyan highlighted cells indicate the pixels of a single micro-lens image. Then, the highlighted green pixels correspond to those that would be used to construct a sub-aperture image. The rays intersecting each of those pixels originate at the same location on the objective optic.

light field data can be manipulated to create images from synthetic cameras with different geometries. However, this thesis will only consider digital refocusing to sensor planes orthogonal to the optic axis. The synthetic imaging equation is derived from considering the geometry of rays propagating within the camera and using basic radiometry to calculate the irradiance that would occur at the synthetic imaging planes [11]. The synthetic imaging equation is

$$E_{(\alpha \cdot f_0)}\left(x', y'\right) = \frac{1}{\alpha^2 f_0^2} \int\int L_F^{(u,v)} \left(u \cdot \left(1 - \frac{1}{\alpha}\right) + \frac{x'}{\alpha}, v \cdot \left(1 - \frac{1}{\alpha}\right) + \frac{y'}{\alpha} \right) dudv \quad (8)$$

where the $\alpha = f_\lambda / f_0$, the scaling factor between the actual and synthetic focal planes. The irradiance, E, describes the power per detector plane surface area and the radiance, L, is the power per surface area per unit steradian. In a sense, radiance describes the contribution of each ray of the light field. The radiance can be related to the photon flux and irradiance by the "cosine to the fourth law" [28, 50].

However, in this case the paraxial approximation is used, so the cosine term is eliminated from the expression. An integral photography method that has been used in the past to compute this equation is adding scaled, shifted versions of the sub-aperture images [11]. This concept can be demonstrated by considering an array of sub-aperture images. Note that each sub-aperture image's depth of field is proportional to the number of sensor pixels within each micro-image [20]. When all the sub-aperture images are added, the result is blurring of objects that are slightly shifted in parallax from one image to the next. In his dissertation, Ng demonstrates this light field property by showing the refocusing operation with just two sub-aperture images [11]. The digital refocusing concept can also be understood graphically by returning to geometrical optics and the associated ray space diagrams previously introduced. As shown in Fig. 8, the refocusing algorithm is essentially calculating a single pixel in the rendered image from adding the detector pixels that sample the sloped line of rays indicated in the ray-space plot. Remembering that the sub-aperture images are represented by horizontal rectangular regions in ray-space, shifting each sub-aperture image will vertically align the points in the figure. The degree of shift in the x-dimension per angular

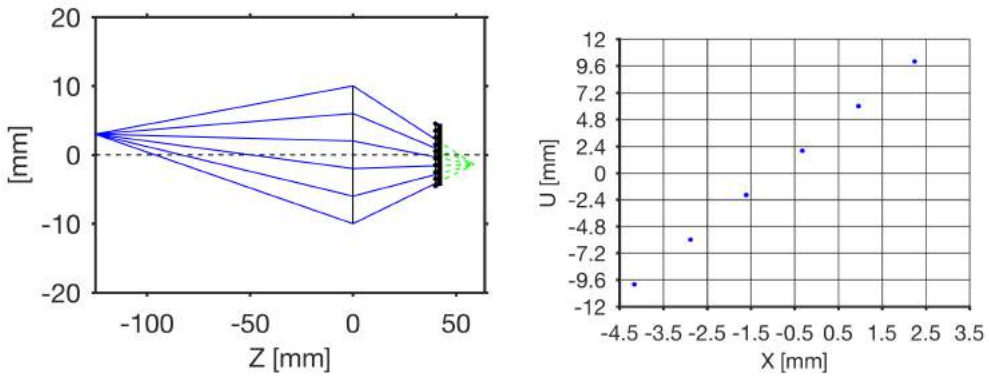

Figure 8. The focused point in the synthetic image plane, indicated by the dashed green line, corresponds to the rays indicated on the ray-space plot. Digital refocusing can be represented as shifting and adding each sub-aperture image so all the points in the ray-space plot are vertically aligned.

sample, or the inverse slope of the line formed by the points in the ray space plot of Fig. 8, can be expressed as $1 - 1/\alpha$ [11, 10]. This type of refocusing algorithm will be referred to as a shear transform. An interesting extension of the digital refocusing process is creating extended depth of field images. This is accomplished from computing refocused images for several synthetic image planes and retaining those sections of the image with sharp features [11]. This may be a useful technique for conducting panchromatic imaging over broad bandwidths using FZP-type optics.

Recent work related to plenoptic cameras has considered the performance of a generalized design where the micro-lens array is not positioned at the objective optic's focal plane. This can be done to trade angular resolution for increased spatial resolution [10, 11, 27]. Much of the angular resolution can be recovered computationally from prior knowledge of the scene. While other light field camera designs should work with the imaging concept presented here, this thesis restricts its scope to considering the traditional plenoptic camera design.

As mentioned earlier, the method of integral photography being proposed in this thesis closely resembles current efforts in LFM [12, 29]. In those applications, the light field is being used to generate a 3-d reconstruction of the scene for the purposes of fluid flow analysis, flame dynamics, or volumetric imaging of weakly scattering specimens. Similar as to what was discussed earlier for photon sieve hyperspectral imaging, a significant challenge for volumetric imaging is isolating the computed imaging plane contributions to only the desired, well-focused elements [30]. In the photon sieve hyperspectral case, the problem arose because of overlapping blurred images from wavelengths not focused at the desired imaging plane. For the volumetric case, this same effect arises because the image at a particular depth includes energy from the out-of-focus elements in adjacent focal planes [30]. Many methods have been investigated to solve this problem and there are several

promising, efficient methods. One example that has demonstrated high efficiency uses frequency-domain deconvolution methods to eliminate the blur [29]. Similarly, the method used in this thesis is based on 3-d deconvolution concepts presented in [12]. This subject is certainly an area that warrants further investigation for application of the FZLFSI. Further discussion of the digital refocusing and deconvolution algorithms used in this thesis is presented in the next chapter.

2.3 Fresnel Zone Light Field Spectral Imager

An overview of the FZLFSI concept is presented in Fig. 9. As shown by Eq. 3, the image formation plane depth for this system is inversely proportional to the incident wavelength. Therefore, the same refocusing algorithms originally developed for modifying the synthetic focused object depth will be applied to imaging at discrete wavelengths. In this system, digital refocusing will allow the computation of separate images at specific wavelengths from the light field recorded in a single exposure. The same general concept of combining an axial dispersion lens with light field camera designs has been recently proposed and simulated in [8].

The performance of such a system can be predicted from considering the limitations of both the FZP and light field camera components. The spatial and

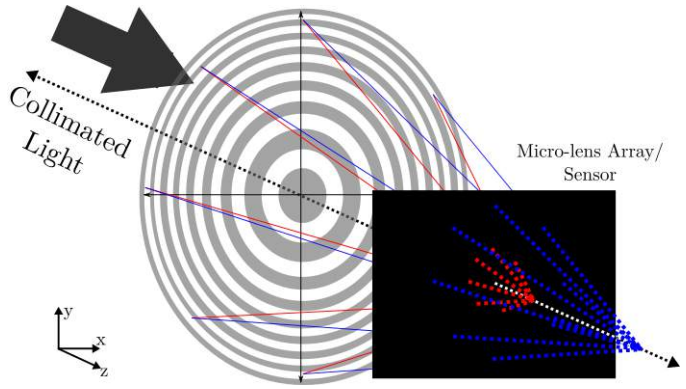

Figure 9. The FZP provides axial dispersion and the light field camera components will allow refocusing to synthetic image planes defined by wavelength.

spectral resolution of FZP-type optics is typically very good, but the the light field camera concept limits how finely the spatial and spectral dimensions are sampled. In this system, the instantaneous field of view (IFOV) depends on the size of the micro-lenses which defines the rendered image "macro-pixels." Smaller micro-lenses will correspond to greater spatial and spectral resolutions. However, as mentioned in Sec. 2.2, there will inevitably be a trade-off. Smaller micro-lenses will also mean reduced angular sampling and thus, spectral range. The next chapter describes the concept in more detail and presents simulations of the system.

III. Simulation

This chapter discusses the system in detail, modeling the system both geometrically and through wave optics. The geometrical model is the best way to demonstrate the general concept, and it provides insight into the relationships between particular design parameters. In developing the geometrical optics model, the FZP was modeled by a thin-lens matrix with a focal length determined by the FZP equations introduced in Section 2.1. However, geometrical optics is inadequate for truly modeling diffraction phenomena which arise entirely from the wave nature of light. While the geometrical model provides a simple approximation, wave optics is needed to fully describe the system's behavior. Therefore, a wave optics model was developed and provides a more robust simulation of the expected imaging performance, given ideal optical components and pure, monochromatic illumination. Together, the two methods of simulation successfully demonstrate this imaging concept and identify the factors that will determine spatial and spectral sampling rates. The development and basic performance of the computational simulations will be presented in this section, but detailed analysis of the results are discussed alongside experimental findings in Chapter 5.

3.1 Geometrical Optics Model

The majority of light field camera literature employs geometrical optics since the light field is a function that essentially describes the radiance distribution across specific rays within the camera. While the geometrical approach definitely has its limitations, it provides useful insight into system fundamentals. The geometrical model in this paper was developed using matrix optics methods to model each optical component and propagate rays through the device. The system was

described using a combination of transfer matrices and thin lens matrices. The transfer matrix is defined as $\begin{bmatrix} 1 & d \\ 0 & 1 \end{bmatrix}$, where d is propagation distance, and the thin lens matrix is $\begin{bmatrix} 1 & 0 \\ -\frac{1}{f} & 1 \end{bmatrix}$, where f is the focal length [31]. These matrices operate on rays expressed in the form $\begin{bmatrix} r \\ \theta \end{bmatrix}$, where r is the lateral position of the ray and θ is the ray angle, relative to the optical axis. The FZP was approximated by the thin lens matrix with a focal length that varies with wavelength, and to better account for the FZP's binary structure, only rays passing through the transparent regions of the zone plate were traced, as shown in Fig. 10. The separation between the micro-lens array (MLA) and the FZP was held constant at the design focal length for the zone plate. Likewise, the detector plane was separated from the MLA by a single micro-lens focal length, f_μ. Each micro-lens was modeled by the thin lens matrix. The matrix equation describing the propagation of a single ray through the

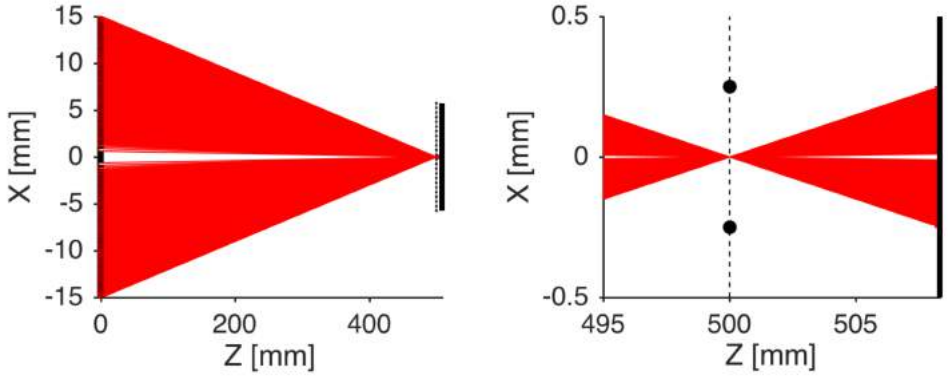

Figure 10. The basic geometrical model of the FZLFSI showing (left) the entire camera set-up and (right) a magnified view of the micro-lens array and detector for a focused wavelength. Only rays passing through transparent regions of the FZP are traced through the system. The dots indicate micro-lens boundaries. The FZP structure causes non-uniform illumination of the micro-lens images.

system displayed in Fig. 10 is

$$\begin{bmatrix} r_{out} \\ \theta_{out} \end{bmatrix} = \begin{bmatrix} 1 & f_\mu \\ 0 & 1 \end{bmatrix} \begin{bmatrix} 1 & 0 \\ -\frac{1}{f_\mu} & 1 \end{bmatrix} \begin{bmatrix} 1 & f_0 \\ 0 & 1 \end{bmatrix} \begin{bmatrix} 1 & 0 \\ -\frac{1}{f_\lambda} & 1 \end{bmatrix} \begin{bmatrix} r_{in} \\ \theta_{in} \end{bmatrix}. \tag{9}$$

Including the dispersion of the zone plate, as described in Section 2.1, f_λ depends on the propagating wavelength as expressed in Eq. 3. As written, the equation is only valid for the center micro-lens, which shares its optical axis with the FZP. In order to correctly model the propagation, the coordinates for the set of rays that intersected a particular micro-lens were transfomed at the MLA plane to a new coordinate system defined by each micro-lens's optical axis. Then, the transformed rays were multiplied by the micro-lens refraction and transfer matrices. This model was computed and displayed using MATLAB®.

The geometrical model is useful for estimating the spectral sampling characteristics of the FZLFSI. The dispersion of the FZP is axial, so the spectral resolution will depend on both the spatial and angular sampling characteristics of the light field detector components. For wavelengths close to the design wavelength, the spatial sampling rate limits the spectral resolution of this system. In this region, spectral differences will not be well-detected until the circle of confusion for the unfocused wavelength exceeds the micro-lens width (Fig. 11). Considered from the digital refocusing process standpoint for a point source, this condition must be

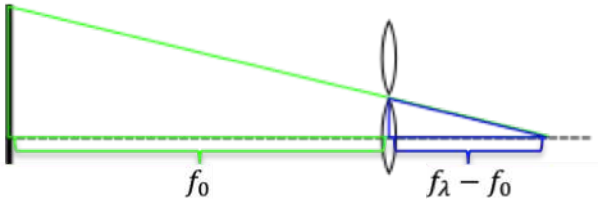

Figure 11. Similar triangles can be used to estimate the minimum change in wavelength that will be well detected by the FZLFSI. The micro-lenses are assumed to be negligibly thin and positioned at the design focal length, f_0. The quantity f_λ is the focal length for the wavelength whose circle of confusion will equate to the micro-lens width.

satisfied for more than just the central pixel in each sub-aperture image to be illuminated. The spectral sampling limit can be described mathematically by considering similar triangles formed by considering the closest detectable unfocused wavelength. One triangle is formed from the FZP radius and the focal length for the wavelength of interest (f_λ), and the other triangle by the difference in focal lengths and the micro-lens radius. This leads to the condition

$$|\lambda| > \lambda_0 \left(\frac{W_\mu}{W_{ZP}} \right) \tag{10}$$

where W_μ and W_{ZP} are the diameters of the micro-lens and FZP respectively. This expression predicts a minimum wavelength difference of 13nm is required to satisfy this condition in the prototype system that will be experimentally demonstrated. The prototype system uses 0.5mm width micro-lenses and a 30mm FZP designed for 800nm. The sampling rate used here is relaxed slightly to 15nm to ensure a strong, detectable response in the adjacent micro-lens images. This sampling rate is demonstrated for two wavelengths close to the FZP design wavelength in Fig. 12. Clearly micro-lens width significantly effects spectral sampling near the design wavelength, but another important condition applies for wavelengths far separated from the design. In these cases, the angular sampling becomes the dominant factor for spectral resolution as shown in Fig. 13. In this region, the synthetic imaging depths are much larger than the design focal length and thus changes to the synthetic focal length do not stimulate as much of a difference in light field response. A useful representation of the spectral sampling trends comes from considering the rays that would achieve focus at synthetic focal lengths separated by 15nm across the detector's range. Fig. 14 shows that as the wavelength decreases below 700nm, the angular sampling rate becomes a more significant factor for distinguishing between the spectral components. Then, as wavelength continues to

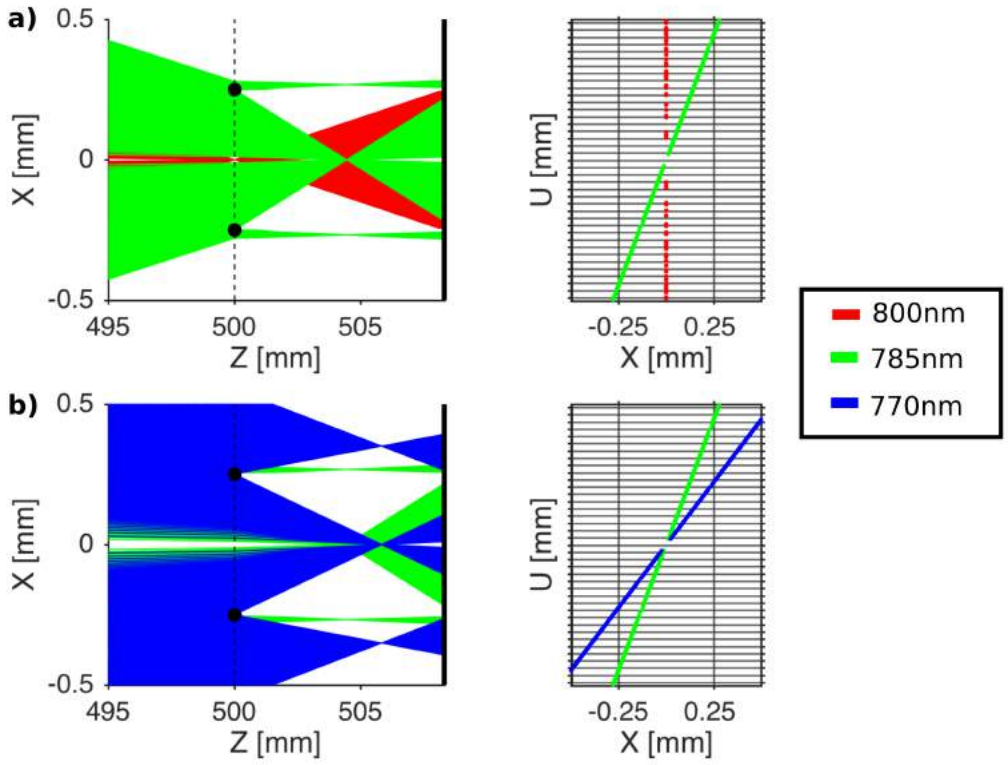

Figure 12. Spectral changes will only be well detected when the wavelength's circle of confusion exceeds the micro-lens width. A spectral separation of at least 15nm is needed for a significant change in the light field pattern indicated by geometrical optics. The effects for a point source emitting different wavelengths focused by the camera is shown in a) for 800nm (red) and 785nm (green). Row b) shows the effect for 785nm (green) and 770nm (blue). The plots in the column on the right are the rays projected into ray-space coordinates where each grid cell represents a detector pixel.

decrease, the angular sampling rate becomes the dominant factor that limits the spectral resolution. For the system modeled, beyond 400nm the degree of angular sampling is certainly inadequate to maintain 15nm spectral bins. Beyond this point, the two different focal lengths are sampled nearly evenly by the same pixels across the entire light field response.

The geometrical approach to modeling this system does not accurately describe the diffraction effects of the FZP and it is useful to discuss some of these limitations before moving on. In Section 2.1 the Huygens-Fresnel principle was introduced to describe FZP function. From this description, if each point across a transparent

Fresnel half-period zone acts as a secondary emitter, there are more rays within the system than the first diffraction order, which results in strong constructive interference at the primary imaging focal plane. This effect is demonstrated by Eq. 6 where there are multiple axial focal points arising from higher orders of diffraction. The first order diffraction response is the desired component of the signal we want to sample in the measured light field. For a conventional refractive lens, the rays, after passing through the optic, are well approximated by one-to-one correspondence with incident rays, but with diffractive optics this approximation is no longer appropriate. There is zeroth order, direct transmission as well as multiple higher orders of diffraction. The geometrical model fails to describe how other diffraction orders will interact with the light field detector assembly, and wave optics modeling of the system is needed to demonstrate these effects.

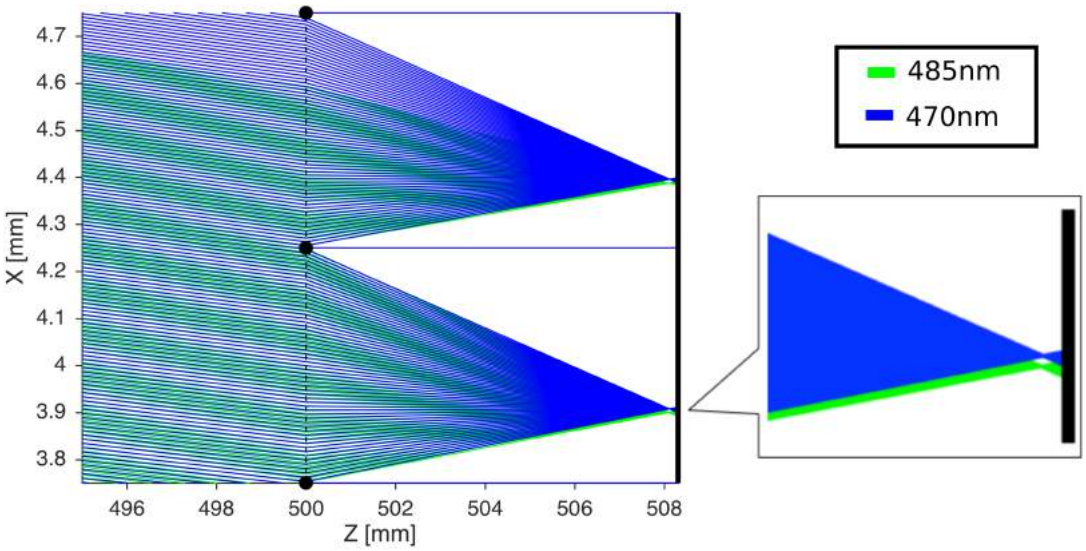

Figure 13. For point sources emitting at wavelengths far from the design wavelength, the light field is focused to small regions within the micro-lens images. As wavelength changes, these illuminated regions shift most significantly in the outermost micro-lens images and angular sampling will determine if the wavelengths are resolved. This figure shows the geometrical prediction for 485nm (green) and 470nm (blue) wavelengths, indicating a high angular sampling rate is required to resolve these wavelengths.

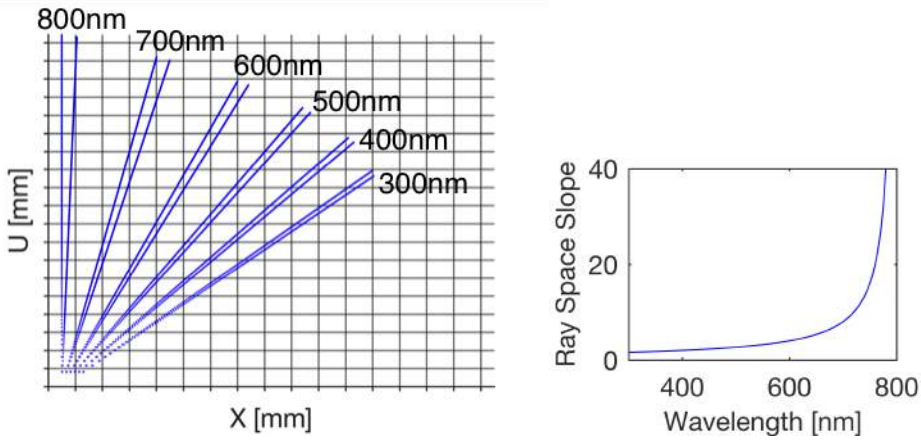

Figure 14. The rays collected by the light field camera to focus at two spectral focal lengths separated by 15nm is demonstrated at 100nm increments across the spectral range. Each ray is plotted as a point in ray space coordinates. The grid represents how these rays are sampled. Each column represents a single micro-lens image and each cell in a column represents a detector pixel. Only one quadrant of the full ray space plot is shown to magnify the sampling characteristics as wavelength varies. The plot on the right shows the slope of the rays projected in ray space coordinates decreases asymptotically to 1 as wavelength decreases. The rate of change of the slope decreases with wavelength which contributes to limiting the spectral bandwidth for maintaining a 15nm sampling interval.

3.2 Wave Optics Model

Diffraction is fundamentally an effect due to the wave nature of light. Therefore, in order to accurately simulate the FZLFSI, a wave optics model is required. The wave optics model developed for this thesis simulates monochromatic imaging. Images with different spectral components are simulated independently by wavelength, then superimposed to form the measured light field. The simulation presented uses the Fresnel approximation and should only be used for systems that satisfy the conditions discussed later in the paper. This section will begin with presenting the forward light field imaging problem given a known spectral data cube. The light fields collected by this type of imager demonstrate a unique character not observed in traditional plenoptic cameras and these qualities will be introduced. Then, the inverse problem will be addressed along with how it was implemented for this study. Standard light field digital refocusing algorithms were

used for computing images at different image formation planes. Then, in the spectral dimension, signatures for isolated pixels were calculated using both digital refocusing and a 3-d deconvolution method.

Forward problem.

Fundamentally, the entire system is not well approximated as shift invariant, and the light field point spread function (PSF) is unique for each point across the detector array [30]. The light field PSF is more complicated than the PSF of a conventional camera because it includes the response of the MLA. Therefore, the PSF is not necessarily a power distribution localized to a specific region on the detector plane, but instead includes the response from each micro-lens image formed beneath the MLA. Since the system will be considered shift variant, it is more accurately expressed by the more generalized superposition

$$F(\mathbf{s}) = \int\int h^2(\mathbf{s}, \lambda, \mathbf{p}) E(\lambda, \mathbf{p}) d\lambda d\mathbf{p} \tag{11}$$

where F is the light field irradiance at a position on the detector described by the vector $\mathbf{s}$. The term h^2 is the light field PSF unique to a single detector location, object point at vector $\mathbf{p}$, and discrete wavelength λ. Finally, the term E represents the true spectral irradiance being imaged, evaluated at a particular wavelength and spatial location. The discrete modeling concepts presented in [12] for volumetric imaging in LFM were modified for the system in this thesis allowing this superposition to be re-cast in the matrix form

$$\mathbf{F} = H\mathbf{E} \tag{12}$$

where H is a measurement matrix whose coefficients are defined by

$$h_{s_i\lambda_j p_k} = \int_{\alpha_i}\int_{\beta_j}\int_{\gamma_k} h(\mathbf{s},\lambda,\mathbf{p})^2 d\lambda d\mathbf{p} d\mathbf{s}. \tag{13}$$

The previous equation represents the discrete elements of the light field PSF, where α_i is the area for the i^{th} detector pixel, β_j is the area of the j^{th} object pixel, and γ_k is the k^{th} spectral bin. An expanded representation of the matrix equation is

$$\begin{array}{ccc} \mathbf{F} = & & H\,[n \times (k \times m)\ \ elements] \quad \mathbf{E} \end{array}$$

$$\begin{bmatrix} F_{s_1} \\ F_{s_2} \\ F_{s_3} \\ . \\ . \\ . \\ F_{s_n} \end{bmatrix} = \begin{bmatrix} h_{s_1\lambda_1 p_1} & h_{s_1\lambda_1 p_2} & h_{s_1\lambda_1 p_3} & ... & h_{s_1\lambda_m p_k} \\ h_{s_2\lambda_1 p_1} & h_{s_2\lambda_1 p_2} & h_{s_2\lambda_1 p_3} & ... & h_{s_2\lambda_m p_k} \\ h_{s_3\lambda_1 p_1} & h_{s_3\lambda_1 p_2} & h_{s_3\lambda_1 p_3} & ... & h_{s_3\lambda_m p_k} \\ . & . & . & & . \\ . & . & . & & . \\ . & . & . & & . \\ h_{s_n\lambda_1 p_1} & h_{s_n\lambda_1 p_2} & h_{s_n\lambda_1 p_3} & ... & h_{s_n\lambda_m p_k} \end{bmatrix} \begin{bmatrix} E_{\lambda_1 p_1} \\ E_{\lambda_1 p_2} \\ E_{\lambda_1 p_3} \\ . \\ . \\ . \\ E_{\lambda_m p_k} \end{bmatrix}. \tag{14}$$

The measured detector response, F, and spectral structure of the object, E, have been re-cast into vector forms to simplify the mathematical expression. Given this set-up, each column of H represents the light field PSF for a particular spectral bin and object pixel. Each row represents the back projection of how much each component of the spectral data cube influences a particular pixel of the measured light field [12]. This expression is consistent with the method used in [8] to model spectral imaging in light field cameras with axial dispersion optics.

The simulation in this thesis was developed to compute the light field PSF for particular spectral elements, the columns of H. This was accomplished in two steps. First, the FZP was modeled by adapting the development of the PSF for a simple

lens found in Goodman [32, p. 110]. Then, the MLA modifies the phase of the field focused at the array, which then propagates a small distance to the detector plane. The reference planes used in deriving the impulse response are shown in Fig. 15.

The field from a unit amplitude point source positioned at (ξ, η) in the object plane propagated to the front of the zone plate, using the paraxial approximation is

$$U_{ZP}(u,v) = \frac{1}{i\lambda z_1} exp\left\{ i\frac{k}{2z_1}\left[(u-\xi)^2 + (v-\eta)^2\right]\right\}. \tag{15}$$

In this equation, z_1 equals the distance from the point source and (u, v) represents coordinates at the FZP plane [32, p. 110]. Then, the wave passes through what can be thought of as an array of apertures, the open rings of the FZP structure. The field after the zone plate becomes $U'_{ZP} = U_{ZP} \cdot P_{ZP}$ where P_{ZP} is the pupil function that represents the FZP's binary structure. Next, the field propagates to the micro-lens array. Using the Fresnel diffraction equation, the field, or impulse

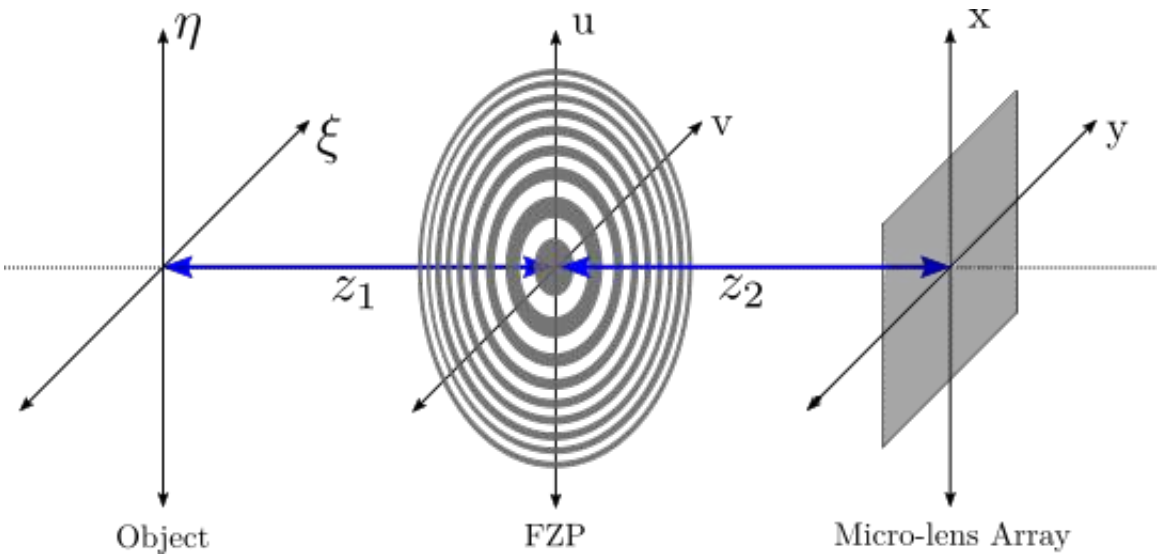

Figure 15. A diagram of the set-up being considered for calculating the FZP PSF with labels corresponding to the equations used throughout this section. The distance from the object plane is represented by the variable z1 and the distance to the micro-lens array is z2. The labels for each axis will be used in the text as the variables representing the coordinates defining the wave amplitude and phase across each reference plane.

response, becomes

$$h_{ZP}(x,y;\xi,\eta) = \frac{1}{i\lambda z_2}\iint U'_{ZP}(u,v)\, exp\left\{i\frac{k}{2z_2}\left[(x-u)^2+(y-v)^2\right]\right\} dudv. \quad (16)$$

Combining Eq. 15 and Eq. 16 results in the expression

$$\begin{aligned} h_{ZP}(x,y;\xi,\eta) &= \frac{1}{\lambda^2 z_1 z_2} exp\left\{i\frac{k}{2z_1}\left(\xi^2+\eta^2\right)\right\} exp\left\{i\frac{k}{2z_2}\left(x^2+y^2\right)\right\} \quad (17)\\ &\iint P_{ZP}(u,v)\, exp\left\{-i\frac{2\pi}{\lambda}\left[\frac{1}{z_1}(\xi u+\eta v)+\frac{1}{z_2}(xu+vy)\right]\right\}\\ &exp\left\{i\frac{k}{2}\left(\frac{1}{z_1}+\frac{1}{z_2}\right)\left(u^2+v^2\right)\right\} dudv \end{aligned}$$

Further simplification is needed to make this expression tractable. The magnification of the imaging system based on geometrical optics can be written as $M = -z_2/z_1$. Substitution into the above equation and combining like terms yields

$$\begin{aligned} h_{ZP}(x,y;\xi,\eta) &= \frac{1}{\lambda^2 z_1 z_2} exp\left\{i\frac{\pi}{\lambda z_1}\left(\xi^2+\eta^2\right)\right\} exp\left\{i\frac{\pi}{\lambda z_2}\left(x^2+y^2\right)\right\} \quad (18)\\ &\iint P_{ZP}(u,v)\, exp\left\{-i\frac{2\pi}{\lambda z_2}\left[(x-M\xi)u+(y-M\eta)v\right]\right\}\\ &exp\left\{i\frac{\pi}{\lambda}\left(\frac{1}{z_1}+\frac{1}{z_2}\right)\left(u^2+v^2\right)\right\} dudv. \end{aligned}$$

The first quadratic phase factor depends on object coordinates (ξ,η) and can be ignored for $z_1 \to \infty$, one of the initial assumptions for this project. The other quadratic phase factor depends on image coordinates and will be retained. This factor is kept in order to retain the phase characteristics of the field for propagation through the micro-lens array. Finally, defining $\widetilde{h} = \frac{1}{|M|}h$ and performing the change of variables $\widetilde{u} = u/\lambda z_2$ and $\widetilde{v} = v/\lambda z_2$ presents a different representation of the impulse response in Eq. 18 that now relates it to the Fourier transform of a scaled

pupil function multiplied by additional phase factors.

$$\begin{aligned}\widetilde{h}(x,y) &= exp\left\{i\frac{\pi}{\lambda z_2}\left(x^2+y^2\right)\right\} \\ &\iint P_{ZP}\left(\lambda z_2\widetilde{u},\lambda z_2\widetilde{v}\right) exp\left\{i\frac{\pi}{\lambda}\left(\frac{1}{z_1}+\frac{1}{z_2}\right)\left[\left(\lambda z_2\widetilde{u}\right)^2+\left(\lambda z_2\widetilde{v}\right)^2\right]\right\} \\ &exp\left\{-i2\pi\left(x\widetilde{u}+y\widetilde{v}\right)\right\} d\widetilde{u}d\widetilde{v}\end{aligned} \tag{19}$$

Eq. 19 was checked for accuracy by plotting the FZP's simulated PSF at the MLA plane against the analytic expression for a zone plate with the given parameters (Fig. 16). Given this impulse response for the FZP part of the system, the object to field formed at the MLA relationship becomes

$$U_{MLA}(x,y) = \widetilde{h}(x,y) \otimes \frac{1}{|M|} U_0\left(\frac{x}{M},\frac{y}{M}\right). \tag{20}$$

The second term in this convolution is simply the geometrical optics prediction for image formation. Moving forward, these expressions are used to calculate the field formed at the MLA, then the light interacts with the micro-lenses and propagates to

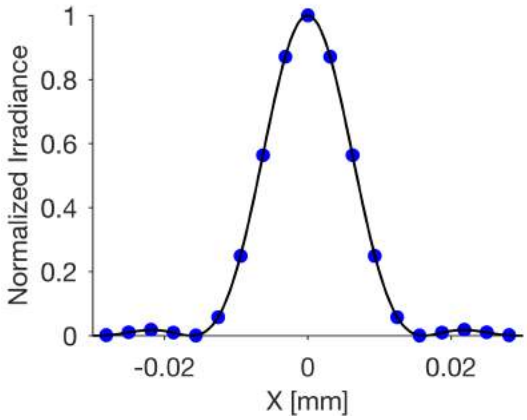

Figure 16. The simulated irradiance at the micro-lens array from a focused point source at optical infinity agrees with what is expected analytically for a FZP. The simulation results, indicated by the blue dots, were computed using Eq. 19 for a FZP with a 30mm diameter and 500mm focal length. The solid line is a plot of the Airy function defined by the same parameters.

the detector plane.

The micro-lens array acts on the field contributed by the FZP by adding another quadratic phase factor specific to each micro-lens. Staying within the paraxial approximation, a lens transforms an incident field with a quadratic phase factor that modifies a wavefront to converge towards the lens's focal point [32, p. 100]. The micro-lens array can be modeled by a comb function, defined by the center point of each micro-lens, convolved with the quadratic phase factor expression that a single micro-lens applies to the incident wavefront. After the micro-lens array, the Fresnel diffraction equation is again used to propagate over the distance from the micro-lens array to the detector array. Combining this effect with Eq. 20 yields

$$\begin{aligned} U_f(s,t) &= \iint \left\{ exp\left[-i\frac{k}{2f_\mu}\left(x^2+y^2\right)\right] P_\mu(x,y)\right\} \otimes comb\left(\frac{x}{W_\mu},\frac{y}{W_\mu}\right) \\ &\quad \iint \frac{1}{|M|} U_0(\xi,\eta)\,\widetilde{h}(x-M\xi,y-M\eta)\,d\xi d\eta \\ &\quad exp\left\{ i\frac{k}{2z_2}\left(x^2+y^2\right)\right\} exp\left\{ -ik\left[\left(\frac{u}{z_2}+\frac{s}{f_\mu}\right)x+\left(\frac{v}{z_2}+\frac{t}{f_\mu}\right)y\right]\right\} dxdy. \end{aligned} \tag{21}$$

In this expression, $U_f(s,t)$ represents the field formed at a particular location on the detector plane. Ultimately, the quantity of interest for simulation will be the irradiance at the sensor plane. The irradiance is calculated by taking the square magnitude of Eq. 21. Rearranged slightly, the final expression becomes

$$\begin{aligned} F_\lambda(s,t) &= \iint \frac{1}{|M|} E_0(\xi,\eta) \\ &\quad \left| \iint \left\{ exp\left[-i\frac{k}{2f_\mu}\left(x^2+y^2\right)\right] P_\mu(x,y)\right\} \otimes comb\left(\frac{x}{W_\mu},\frac{y}{W_\mu}\right) \right. \\ &\quad \left. \widetilde{h}(x-M\xi,y-M\eta)\, exp\left\{ -ik\left[\left(\frac{u}{z_2}+\frac{s}{f_\mu}\right)x+\left(\frac{v}{z_2}+\frac{t}{f_\mu}\right)y\right]\right\}\right|^2 dxdyd\xi d\eta, \end{aligned} \tag{22}$$

where F_λ represents the light field response for imaging an object at a particular wavelength. A similar development is accomplished by Shroff and Berkner for

standard plenoptic imaging systems, and their result is consistent with Eq. 22 [33]. The algorithm used considers each object pixel separately for propagation through the system, then superposition of the light field PSFs for each element of the object constructs the final result as described by Eq. 14.

The continuous Fourier transforms described in the equations above are computed as discrete Fourier transforms (DFT), so sampling becomes an important consideration. The scaled FZP structure from Eq. 19 must be finely sampled to accurately model the outermost rings. Also, the MLA plane must be sampled with enough precision to accurately simulate the image formed by the FZP. The MLA and FZP planes' sampling requirements directly compete. Coarse sampling of the FZP corresponds to finer sampling at the MLA and vice versa. The sampling rate at the FZP is determined by L, the physical size of the array used to sample the scaled FZP structure divided by N, the number of samples in each dimension, $\delta_{ZP} = \frac{L}{N}$. Then, because the MLA and FZP planes are related by a DFT, the resulting sample size at the MLA is

$$\delta_{MLA} = \frac{1}{N\delta_{ZP}} \tag{23}$$

[34]. The sampling rate at the MLA plane was kept above the maximum spatial resolution of the objective optic. Based on the Nyquist criterion, the sample size for the model was chosen as half the diffraction limited spot size of the FZP. In order to finely sample at the MLA plane, a large physical array size, L, is required to sample the FZP. Increasing physical array size then requires more samples along each dimension to adequately model the fine structure of the outermost rings. These sampling requirements and their associated computational burden may limit the designs that can be simulated with this model. As new FZLFSI design concepts are explored, the computational model should be further improved to efficiently predict

performance.

While the system is not well approximated as translation invariant, it was observed during simulation that the light field PSF exhibits a degree of periodicity. The light field PSF for a source emitting a single wavelength at the point $\left(\frac{\xi}{M}, \frac{\eta}{M}\right)$ is identical to a translated version of the light field PSF for a source at $\left(\frac{1}{M}\left[\xi + aW_\mu\right], \frac{1}{M}\left[\eta + bW_\mu\right]\right)$, for integer values of a and b (Fig. 17). This observation is consistent with wave optics modeling of volumetric imaging in light field microscopy [12]. This means that computing the light field of an object at a discreet wavelength can be efficiently implemented using a convolution operation. This is achieved by first calculating the light field PSF for the particular wavelength. Then, the light field PSF is convolved with a down-sampled representation of the object defined by the criterion for light field PSF periodicity introduced previously. In this way, the computation becomes a limited number of convolution operations defined by the sampling characteristics of a particular micro-lens image. There is a certain degree of spatial translation in object space that is required before a

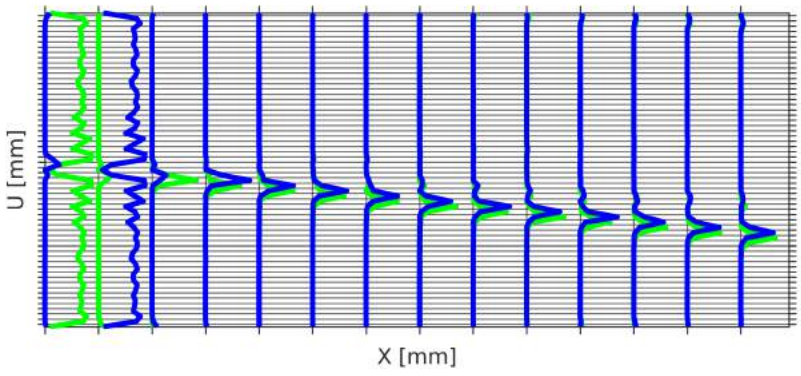

Figure 17. A 1-d ray space projection comparing the simulated light field PSFs for two sources emitting at the FZP's design wavelength. The plotted lines represent the normalized irradiance within the micro-lens images. The columns of the plot represent consecutive micro-lens images and the cells of the grid show the spatial and angular sampling rates. The green and blue traces represent the light field PSFs from sources that are separated by W_μ/M along a chosen dimension. The light field PSFs are identical up to a translation on the detector array of a single micro-lens image. This characteristic also holds for wavelengths other than the design wavelength.

modified light field PSF is detected, as demonstrated in Fig. 18. Another visualization of this quality can be seen in Fig. 6 where closely-spaced object points are almost identically sampled within a single micro-lens image. Detectable variations across the locations sampled by a particular micro-lens will then depend on the pitch of the detector array. This characteristic also indicates that the complete light field can be closely approximated by a single convolution operation corresponding to the object points sampled at the center of each micro-lens. This approximation can simulate the light field response of a monochromatic object in a matter of minutes compared to the direct method which typically requires more than 24 hours to run. The simulations presented in this thesis were primarily computed using the direct method, but the convolution approximation was useful to investigate certain system characteristics throughout the study.

An imaging simulation for a simple object emitting at the design wavelength, 800nm, and then at 740nm is presented in Fig. 19. This figure confirms the simulation generates the expected light field response for focused and unfocused objects. For focused objects, the micro-lens images are uniformly illuminated as was

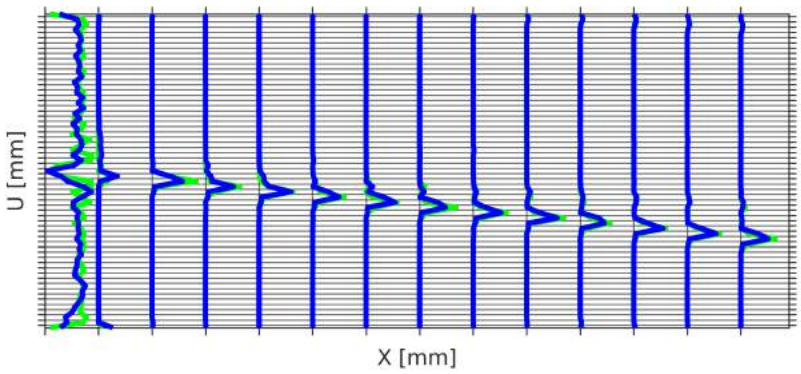

Figure 18. A 1-d ray space projection comparing the simulated light field PSFs for two sources emitting at the FZP's design wavelength and spatially separated by $0.25^{W_\mu}/_{M}$. This shows that there is a minimum amount of spatial separation required between the two sources in object space in order to generate detectable differences in the light field PSFs.

shown geometrically in Fig. 10. Then for the unfocused case, the object's features are sampled across multiple micro-lens images. These expected effects are well demonstrated in Fig. 19. Additionally, the light field presented an unexpected phenomenon, unique to this type of light field camera and not predicted by the geometrical models. Ghost images of the full object are formed in each micro-lens image from zeroth-order, direct transmission and higher orders of diffraction. This effect will be further discussed in Sec. 5.1.

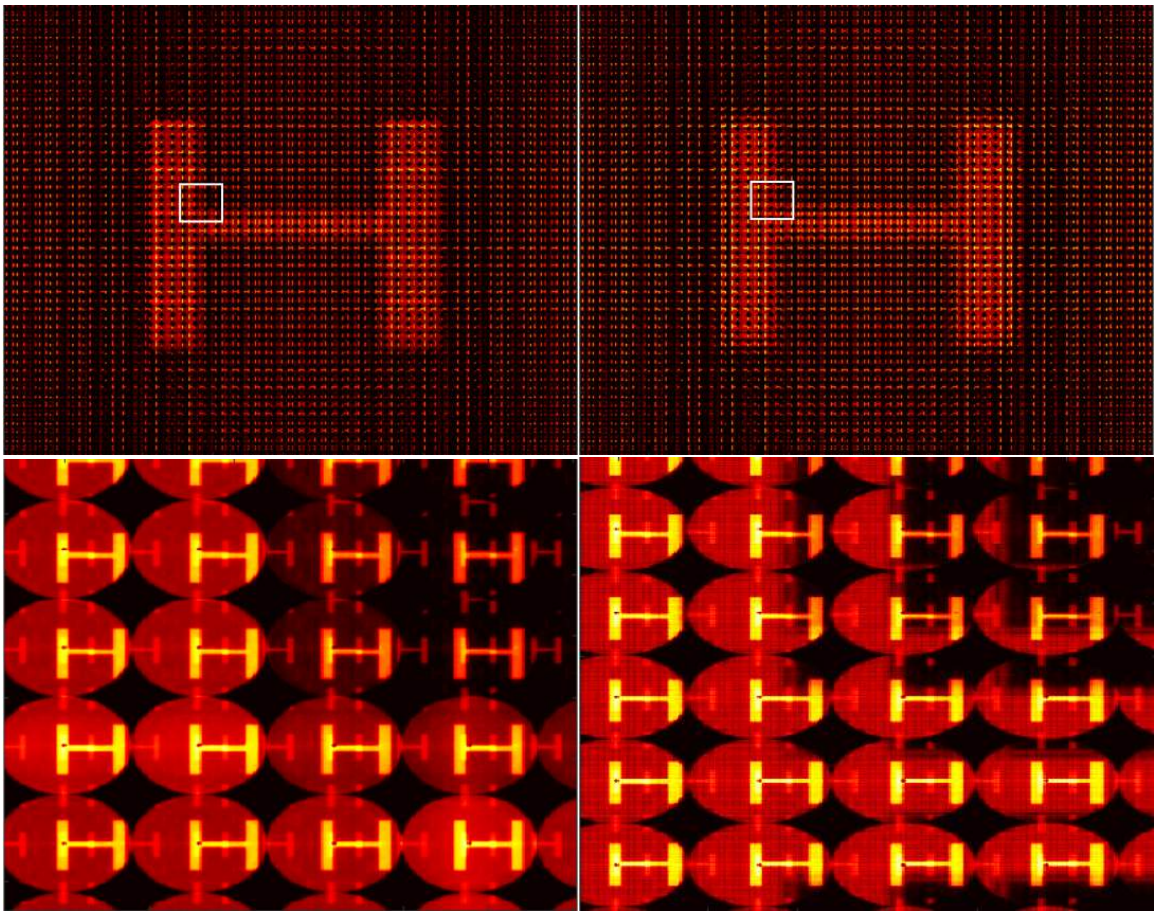

Figure 19. Simulated light fields produced by a f/16.6 FZLFSI with a 500μm pitch MLA. The images on the left show the detector plane response for the focused design wavelength at the micro-lens array. The images on the right are for a shorter, unfocused wavelength at the MLA. With the shorter wavelength, the edge of the H is now sampled across multiple micro-lens images. Also, notice the ghost images of the full object formed in each micro-lens image. These images form from zeroth-order, direct transmission and higher orders of diffraction.

Accuracy of the Fresnel Approximation.

The Fresnel approximation can be described using the Huygen-Fresnel principle defining the secondary emitters at the diffraction plane. The distance from each of these emitters is approximated by keeping only the first two terms of a binomial expansion of the distance equation. The condition to maintain accuracy in this case becomes

$$1 \gg \frac{\pi}{4\lambda z^3}\left[(x-\xi)^2+(y-\eta)^2\right]^2_{max} \tag{24}$$

where z represents the propagation distance, (ξ, η) are source plane coordinates, and (x, y) are in the observation plane [32]. This expression describes that the contribution of the first discarded term of the binomial expansion should be much less than 1 radian to avoid introducing significant error to the phase terms of the propagating field. For propagation from the micro-lens array to the detector, with 500μm diameter micro-lenses and z =8.31mm, this condition is not necessarily well satisfied with a value just less than one. However, another characteristic that has been shown to accurately judge the suitability of the Fresnel approximation is the Fresnel number, $N_F = {}^{r^2}/_{\lambda z}$, where r is the radius of the aperture [35, p. 55]. For the micro-lens propagation, the Fresnel number is close to 20 which has been shown to still provide acceptable results. Additionally, the validity of the Fresnel approximation for the FZP part of the system has been shown in previous studies. The contribution from the first discarded term of the approximation, in this case, is less than or equal to $\pi\lambda/(16f_0)$ [2]. For the simulations in this paper, this term is on the order of 10^{-7}, so the Fresnel approximation is well justified. Accepting the potential for a small amount of error introduced by the Fresnel approximation when propagating from the micro-lens array to the detector, the simulations in this paper provide an excellent prediction of system performance.

Inverse problem.

There are two approaches for approximating solutions to the inverse problem of determining the spectral imaging data cube from the measured light field, digital refocusing and 3D deconvolution. Digital refocusing does not account for the unfocused contributions from wavelengths close to the spectral bin being imaged and provides relatively coarse resolution in the spectral dimension. However, for the purpose of this thesis, digital refocusing performs well for monochromatic imaging and basic demonstration of the system's ability to discriminate between the unique spectral profiles of different light sources. Two digital refocusing techniques used in this thesis are the shear and the Fourier slice algorithms. The shear algorithm is the spatial domain implementation of the synthetic imaging equation, Eq. 8, as conceptually demonstrated in Fig. 8. It can be described as shifting and stacking the sub-aperture images formed from the sampled light field. These sub-aperture images are constructed by using the same relative pixel from each micro-lens image across the array. Then, these images are each shifted based on the depth of the desired synthetic image plane [11]. In this way, the resolution of each sub-aperture image is set by the number of micro-lens images, and thus, the resolution of the final image will depend on the pitch of the MLA. The experimental portion of this project used a MLA with 50x50 micro-lenses, so this significantly limited the resolution of the rendered images. The simulations presented in this section do not necessarily follow this constraint in order to better illustrate the concepts. Figure 20 demonstrates the digital refocusing of a simulated light field from the illumination of unique objects at two discrete wavelengths.

The shearing algorithm is computationally expensive in that its complexity is $O(n^4)$, where n is the number of pixels in the measured light field. However, the shearing operation can be translated to the Fourier domain resulting in a reduced

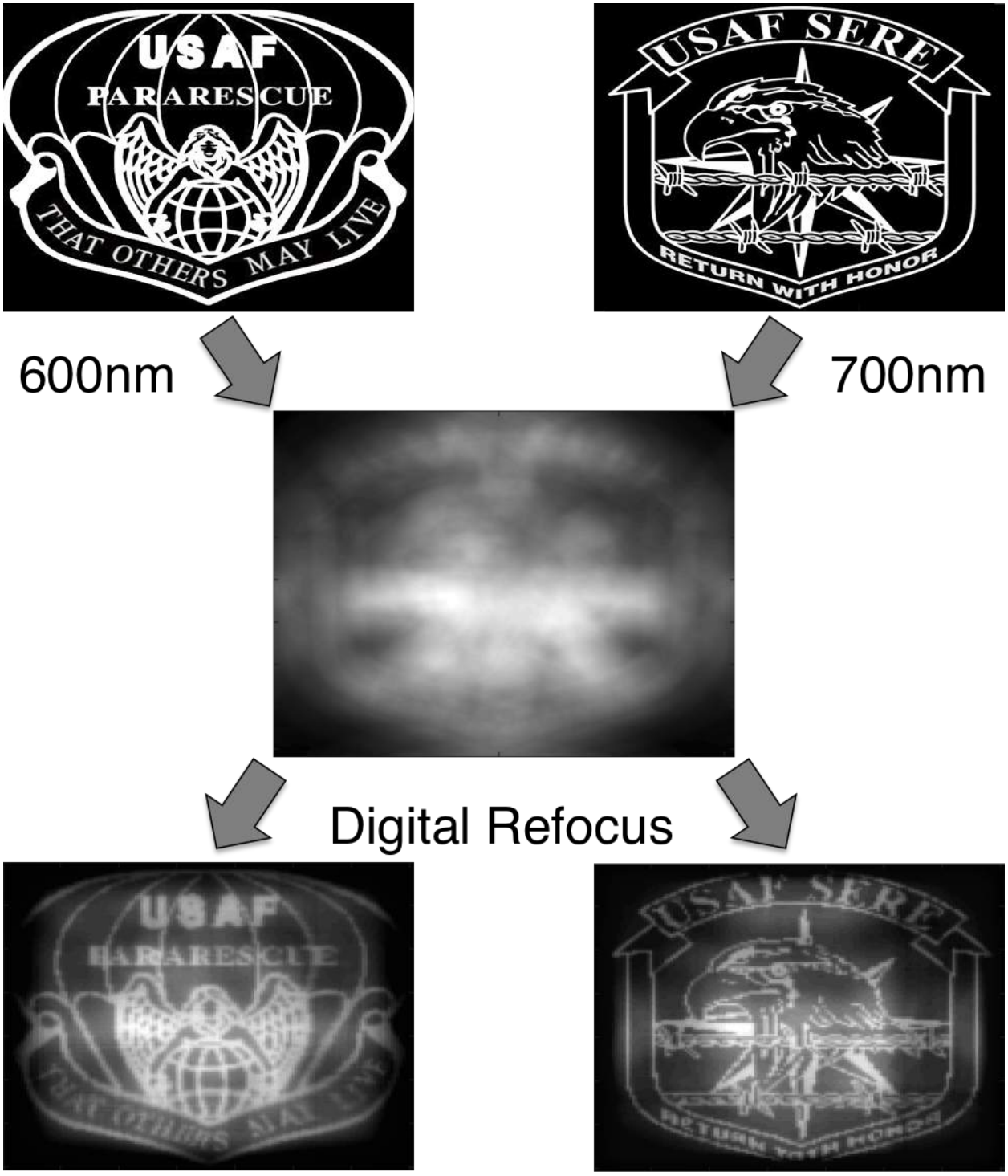

Figure 20. Two different, coplanar objects indicated in the top row, were simulated to emit at discrete wavelengths. Then, the combined signal was collected by a f/13 FZLFSI with a 200μm pitch MLA. The middle picture demonstrates the image formed at the focal plane of the design wavelength for the FZP. This image represents the signal that would be measured in a conventional camera design. In the modeled system, the light field is collected and computationally processed to digitally refocus based on wavelength. The bottom row shows digitally refocused images from the collected light field, refocused to 600nm (left) and 700nm (right).

computational burden with the complexity reduced to $O\left(n^2 \log n\right)$ [36]. This method arises from considering the Fourier transform of Eq. 8. The shearing algorithm in the spatial domain is essentially realigning the angular dimensions of the light field and then adding each ray as shown in Fig. 8. It can be shown that this operation in the frequency domain is equivalent to extracting a slice of the 4-d Fourier transformed light field that is the DC component of the frequencies in the (u, v) dimensions [37]. Mathematically, this is represented as

$$\hat{E}\left(f_{x'}, 0\right) = \int\int L_F\left(u, x'\right) e^{i2\pi f_{x'} x'} du dx' \tag{25}$$

where $\hat{E}$ is the Fourier transform of the refocused image. The Fourier slice algorithm has been shown to compute comparable quality of refocused images to the shear transform. Of interest in this paper is the comparison of how these algorithms perform in the spectral dimension. Figure 21 shows the computed spectral linewidth of a monochromatic point source is consistent for both methods. There are some artifacts in the spectrum computed using the Fourier slice method that may arise from the degree of padding used when computing the 4-d DFT of the light field.

Digital refocusing methods work well for conventional photography, but are not as precise when imaging different layers of a weakly scattering volume, such as in light field microscopy. When imaging a depth in the volume, there are blurred contributions from objects in planes adjacent to the desired depth. This is a significant challenge for volumetric imaging and in concept is very similar to spectral data cube processing from FZLFSI light fields. A method for better isolating images from a single depth, or a single spectral bin, is implementation of a 3-d deconvolution [8]. The most likely estimate for the true volume in LFM, or spectral data cube with this system, can be determined from a Richardson-Lucy iteration scheme using the measurement matrix from Eq. 14 and the collected light field [12].

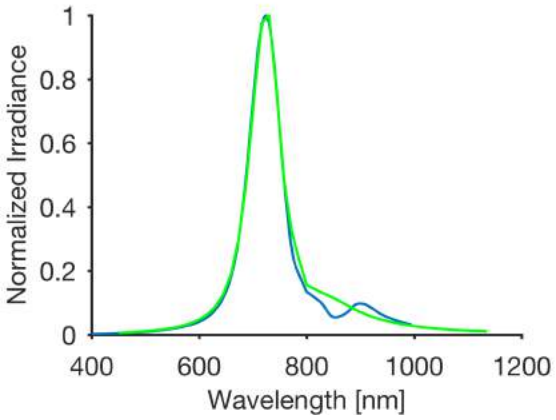

Figure 21. The computed spectral profiles for the shear (green) and Fourier slice (blue) digital refocusing algorithms are compared for a simulated monochromatic point source emitting at 716nm. Rendered images of a monochromatic point source were calculated for 5nm spectral bins across the range. The irradiance for the rendered pixel of the source is shown in the plots. The Fourier slice algorithm was computed without any padding to the light field array and shows a small artifact in the line shape near 900nm.

For the purpose of this paper, this method will be further simplified to only consider deconvolution in the spectral dimension for spatially isolated point sources (Fig. 22). This was implemented by computing the light field PSFs for each spectral bin of the pixel of interest. Then, the built-in MATLAB® Richardson-Lucy deconvolution function was applied to the signal. The inputs to the Richardson-Lucy iteration were the 2-d detector array response and the computed light field PSFs for each spectral bin. Even with this simplification, the deconvolution method is much more precise than the digital refocusing algorithms for computing spectral signatures. A comparison between spectral profiles from a monochromatic point source computed using digital refocusing and the Richardson-Lucy method is shown in Fig. 22. This figure makes it clear that the Richardson-Lucy method is superior for resolving fine spectral features. The algorithms for solving the inverse problem, discussed in this section, are essential to analyzing the experimental performance of the prototype system presented in the next chapter.

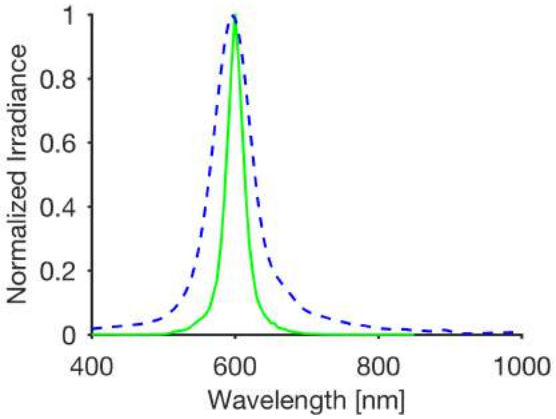

Figure 22. The computed spectral profiles for the digital refocusing (blue) and Richardson-Lucy deconvolution (green) methods are compared for a simulated monochromatic point source emitting at 600nm. The plots show the normalized irradiance of the source's rendered image pixel across the range.

IV. Experiment

This thesis provides experimental demonstration of spectral imaging by a light field camera that uses an axial dispersion lens. In order to demonstrate the device, the light field PSF for the prototype system was measured for several wavelengths, which also confirmed the accuracy of the computer simulations discussed in the previous chapter. Next, synthetic images of a resolution chart with monochromatic illumination were processed for wavelengths across the approximately 100nm tuning range provided by a Ti:Sapphire laser. Finally, the spectral signatures of two calibration lamp point sources were computed to demonstrate the spectral sampling capabilities of the prototype system. The experimental portion was purposely limited in scope to investigate the fundamental aspects of system performance. For example, monochromatic illumination was used to demonstrate digital refocusing by wavelength. Also, when imaging point sources with spectral structure, the sources were well-separated and at the same object depth. This was done to simplify computation of the spectral profiles and minimize spectral cross-talk between pixels. The full implementation of a 3-d deconvolution algorithm would help to account for these effects and could be the focus of future research. It is important to recognize that the experimental constraints were not dictated by fundamental physical limits of the FZLFSI concept. Instead these laboratory control measures were imposed to enable a clear demonstration of the system's optical performance. The scope of the experiment was also limited to the evaluation of basic optical properties and did not include any characterization for the radiometric sensitivity of the prototype system.

The general experimental set-up is shown in Fig. 23. The FZP was set up with an achromatic relay lens (L2) to conduct imaging at optical infinity for the monochromatic imaging and spectral discrimination portions of the experiment. This was required to maintain an image side f/# for the objective optic that

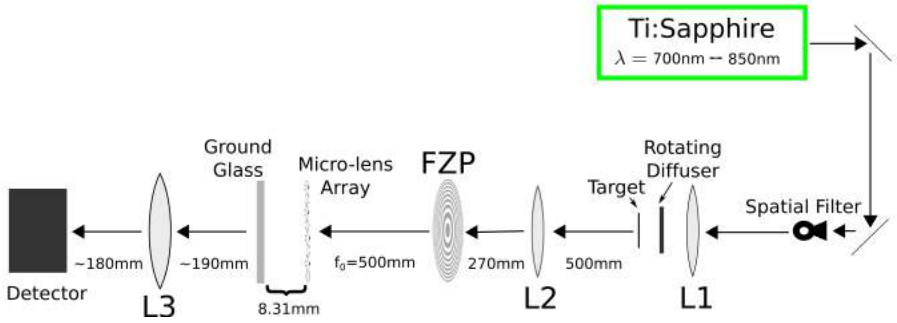

Figure 23. The Ti:Sapphire laser was the primary source of illumination and was spatially filtered then collimated using lens L1. A rotating diffuser was used to provide incoherent illumination of a transparent USAF 1951 resolution target. L2 is a relay lens for the FZP to image the resolution target at optical infinity. The micro-images were projected on ground glass, and L3 is a relay lens to image the ground glass onto the detector array.

matched the micro-lens array configuration. The relay lens was aligned to produce a focused image of a USAF 1951 resolution target at the FZP image plane when the target was illuminated at the zone plate's design wavelength, 800nm. As discussed in Sec. 2.2, the MLA was fixed at the design wavelength's image plane and the detector array should be aligned with the back focal plane of the MLA. However, most commercially available camera assemblies have the detector array recessed within the camera body making the separation of the MLA and detector plane difficult to achieve in the laboratory setting. In these cases, a relay imaging system can be used to image the back focal plane of the MLA [20, 12]. Fine ground glass is placed at the back focal plane to reduce vignetting. During all parts of this experiment, the MLA projected the micro-lens images onto a plate of ground glass that was imaged onto the detector array inside the camera housing using an SLR camera lens as the relay optic. The camera and relay lens were configured to achieve close to 1:1 imaging of the micro-lens images. This also served to maximize coverage of the detector array within the camera. Magnification in the relay imaging system could be used in the future to better investigate the structure of the light field at the ground glass but was not needed for this study.

With the relay imaging system in place, precise alignment of the ground glass and MLA was an important factor, as described in Sec. 2.2. These components were coarsely aligned by imaging a point source located at the FZP plane. The point source was constructed from a fully stopped down iris illuminated by a white-light LED. The separation of the MLA and ground glass was tuned until a focused spot was obtained for each of the micro-lens images. Uniform micro-lens PSF profiles across the array were obtained by adjusting the tilt of the ground glass to ensure the MLA and ground glass were close to parallel. Recall from Fig. 5, these focused points represent the center pixel for each micro-image, and were helpful for confirming the calibration parameters of the algorithm which reshapes the 2-d detector response into a 4-d light field. They help to approximate micro-lens image spacing across the detector array as well as identify any rotational misalignment. Both these characteristics are essential for accurate construction of the 4-d light field. Errors in constructing the light field will degrade both spatial and spectral resolutions obtained by rendered images.

Following this coarse alignment, the separation of the MLA and ground glass were fine tuned by imaging the Ti:Sapphire laser-illuminated resolution target with the FZP as the objective optic. The separation of the MLA and ground glass was adjusted to achieve the sharpest edges within the micro-lens images. Slight variations of the illumination wavelength away from the FZP design wavelength was useful to help identify the resolution target features within the micro-lens images during alignment. The MLA, ground glass, and detector alignment that was done for the prototype system initially was not varied during the remainder of the experiment. With this description of the experimental set-up as a basis, the following section provides more detailed descriptions of the components.

4.1 Equipment

Tunable, CW Ti:Sapphire Laser.

A Spectra-Physics 3900S tunable, continuous wave (CW) Ti:Sapphire laser was used as the illumination source to demonstrate synthetic imaging by wavelength for this prototype system, across the range of wavelengths the laser was capable of generating. The laser cavity was configured with optics that allowed wavelength tuning in the range of 700 to 850nm. The tuning capability of this laser is achieved by placing a birefringent filter inside the cavity to restricts cavity mode resonances to specific wavelengths within this range. The angle of the filter can be finely controlled and thus allows tunable, wavelength dependent modification to the polarization of different modes. Wavelengths not returning to horizontal polarization after a round trip through the birefringent filter are greatly attenuated at the Brewster's windows on both sides of the gain medium [38]. The Ti:Sapphire laser output wavelength was well correlated to the birefringent filter's micrometer settings, so repeated wavelength measurements for specific micrometer settings were not necessary. The output wavelengths were initially measured using a BW Tek Exemplar® spectrometer which has a spectral resolution of 0.5nm [39] and a look-up table for micrometer settings was created from this data.

As the laser output was tuned across this range, the gain medium emission profile is not constant, and maximum intensity is observed near 800nm. This effect caused variations in illumination power across the tuning range. This was not an issue for the experiment since the results did not depend on absolute irradiance. In order to demonstrate monochromatic imaging for this wavelength range, it was only necessary for the detector to be sensitive enough to detect the laser illumination at the lowest irradiance in the range, and it was. For each of the cavity modes across this tuning range, the spectral linewidth of the output beam remains narrow. The

spectral linewidth of the laser is less than around 0.1nm, so for the purposes of this experiment, it was approximated as monochromatic [38].

Along with the spectral response of the laser, the beam quality of the illumination laser is an important factor in characterizing the beam profile used for measuring the light field and zone plate PSFs. At the pump powers used, M^2 values were obtained close to 1.06, as measured using a Coherent, Inc. ModeMaster PC beam profile analyzer. This value indicates the beam profile is well approximated by the Gaussian TEM_{00} mode. The beam was spatially filtered to eliminate higher spatial frequencies, providing a clean signal for interrogating the various optical components. Spatially filtering the beam requires focus through a pinhole just big enough to transmit the waist of the focused beam. This technique is based on the fact that the focal plane of a lens is the Fourier transform plane for the input beam profile [32]. In this way, the pinhole aperture acts as a low-pass filter of the laser beam's spatial profile. The approximate spot size of a Gaussian beam after being focused by a lens is described by the equation

$$w_{02} \approx \frac{\lambda f}{\pi w_{01}} \tag{26}$$

where w_{02} is the spot size at the focus and w_{01} is the beam size just prior to the lens [31, p. 78]. However, in order to maximize the energy transmitted through the pinhole, the diameter is often made larger than this size by neglecting the π factor in the denominator. A pinhole of this size eliminates the majority of the higher spatial frequencies and provides a clean beam profile. For this experimental set-up $w_{02} \approx 5\mu$m and a 10μm pinhole was used for the spatial filter.

After spatially filtering the beam, an achromatic lens was used to produce collimated, uniform illumination of the target. The expansion of the beam at the lens, after the spatial filter, can be determined by comparing the triangles formed

by the marginal rays between the spatial filter's lens and L1. This relationship can be written in terms of the focal lengths of the spatial filter and L1, $f1$ and $f2$ respectively, as

$$w_{03} = \frac{f_2}{f_1} w_{01} \tag{27}$$

where $w_{03}$is the beam diameter at the collimating lens. The collimating lens in this experiment was selected to provide a collimated beam large enough to illuminate enough of the resolution target to adequately demonstrate the prototype system's imaging performance. The achromat used was a Thorlabs AC508-400 lens with a focal length of 400mm.

In addition to spatially uniform illumination of the target, the illuminator beam also needed to be incoherent, so that speckle effects could be precluded. The coherence of the collimated laser beam was disrupted by placing a rotating diffuser immediately before the resolution target. The rotation of the diffuser during measurement eliminates the majority of the coherence effects that would be otherwise observed [32, p. 162]. The rotating diffuser was constructed of a sheet of ground glass rotated by an electric motor at a constant rate. However, a single sheet of ground glass cannot provide perfectly Lambertian illumination, and the diffuser was placed as close to the resolution target as possible to maximize the observed radiance at the imager [40, p. 229].

Calibration Lamp Pinhole Sources.

For characterization of the prototype system's spectral response, Oriel® Instruments spectral calibration lamps were used. The two calibration lamps chosen for this experiment were Hg-Ne and Kr because they demonstrate profiles with significant spectral differences for features with maximum intensity [41]. The two

lamps were shielded so only a pinhole aperture of each was imaged to simplify the computation of spectral profiles, as discussed earlier. During these test runs, the resolution target was removed and the lamps were mounted as close as possible to the same longitudinal location. Realignment of the zone plate's relay lens, L2 in Fig. 23, was not necessary for demonstrating the spectral discrimination capability of the system. This may have introduced small errors in the computed spectral profiles, which were calculated assuming imaging at optical infinity.

Consistent spectral intensity of the calibration lamps over multiple test runs was a concern. The spectral output of the Hg-Ne lamp is sensitive to temperature [41]. In order to maximize the intensities of the desired Ne lines, the lamp needed to be kept cool. It was found that in order to do this, only a three-second run time was used, and the lamp was allowed to fully cool between measurements. For thorough spectral calibration of the detector, a more stable operating condition for the calibration sources should be used. The measured spectral profiles of the calibration lamps for these test conditions are shown in Fig. 24. Spectral profiles were measured using the Exemplar® spectrometer.

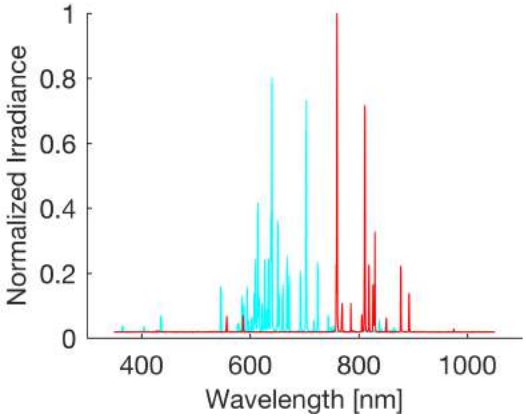

Figure 24. The spectral profiles for the (cyan) Hg-Ne and (red) Kr calibration lamps measured by the spectrometer. The Hg-Ne lamp was kept cool to bring out the Ne lines. This was done by limiting run time to less than 3 seconds for each measurement.

FZP Design and Fabrication.

As described in Sec. 2.2, the image side f/# of the objective optic should be matched with the micro-lenses to maximize the size of micro-lens images on the detector array but without overlapping them. This being the case, the FZP design was constrained to an f/# of 16.62 based on the MLA available for the experiment. Another consideration in establishing the FZP design was the intended spectral range. This study considers the visible and near infrared spectrum, so the design wavelength (λ_0) was chosen as 800nm. The usable area of the rotating diffuser and size of the collimating lens limited the testable FZP diameter to approximately 30mm. Additionally, though not a factor for this study, the diameter of the FZP for a chosen wavelength is ultimately limited by the tolerances of the fabrication technique. As seen by Eq. 4, as the diameter of the optic increases, finer precision is required to accurately print the rings. For the FZP used in the experiment, the narrowest ring width was 10μm which is well within typical fabrication limits. The optic used for this study was manufactured as a photomask by Advance Reproductions. The zone plates were designed using the equations introduced in Sec. 2.1 and encoded in a Gerber file format that was compatible with the manufacturing machines. The FZP was printed on a square, chrome-coated quartz plate using the design file that was created.

The PSF for the FZP was measured to verify its optical performance and identify any fabrication errors. This was accomplished by focusing a collimated, monochromatic beam through the FZP. The focused point was then re-imaged using a microscope objective. The microscope objective and detector were aligned to magnify the focused point by a factor of 100. The HDR scale-and-splice method shown in [24] was used to better image the weak PSF features. Then, the measured response was compared to the simulation of the zone plate's PSF (Fig. 25).

Uncertainties in this PSF measurement arise from imperfect collimation and alignment of the optical system. The quality of the collimation was measured using a shear plate collimation tester, which indicated good collimation with a low-degree of aberration. The measured PSF matched what was predicted. This indicated that the FZP design and fabricated structure were accurate enough for the purposes of this experiment.

Following this verification of FZP performance, the dispersion of the FZP was characterized. The axial chromatic aberration of refractive lenses is commonly expressed in terms of the Abbe number, which is the reciprocal of the dispersive power of the lens. Typically, large Abbe numbers are desired, meaning a low degree of dispersion. However, for this experiment, it is actually necessary for the optical component to have significant, known dispersion, with a relatively low Abbe number. The Abbe number, V_d, can be expressed as

$$V_d = \frac{n_d - 1}{n_F - n_C} \tag{28}$$

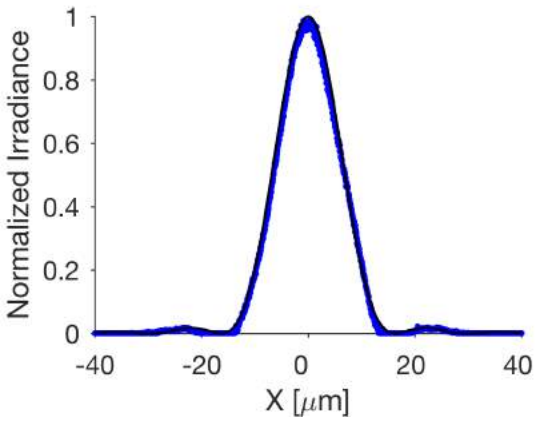

Figure 25. The PSF for the FZP was measured to validate its design and fabrication. The (blue) experimental measurements match the (black) predicted Airy function for this FZP design. The measurements were conducted using a microscope objective to magnify the PSF. Additionally, the scale and slice HDR method in [24] was used to resolve the weak features in the PSF tails.

where the lens material's refractive index, n, is measured at the Fraunhofer lines indicated by the subscripts [22, p. 270]. Measuring the Abbe number for a diffractive optic, such as the FZP, requires modification of this expression using the relationship between the focal length and index of a lens, $\frac{1}{f_\lambda} = [n(\lambda) - 1] C_0$, where C_0 is a constant for the particular diffractive lens [42]. Then, Eq. 3 can be used to relate focal length of a diffractive element to wavelength. These lead to two new expressions for the Abbe number, which were used to characterize the FZP in this thesis

$$V_d = \frac{1}{f_d\left(\frac{1}{f_F} - \frac{1}{f_C}\right)} = \frac{\lambda_d}{\lambda_F - \lambda_C}. \tag{29}$$

The focal lengths were measured experimentally by illuminating the FZP with collimated white light. Then, the spectral focal lengths were measured by using the spectrometer to find the points of maximum irradiance for wavelengths close to the appropriate Fraunhofer lines. The spectrometer was placed behind a fully stopped down iris to limit the unfocused contributions of other wavelengths. Using this method, the Abbe number was experimentally measured as $V_d = -3.51$, close to the predicted value of -3.45. The Abbe number is negative, indicating that blue light focuses to the right of the red, which is the opposite of dispersion in refractive materials. The dispersive power, indicated by the low Abbe number, is much greater than that from refraction in optical glasses where typical Abbe numbers are greater than 25 [22, p. 271]. The predicted Abbe number for the FZP is consistent with what is reported in references [42, 43, 44].

Micro-lens and detector arrays.

The micro-lens array used in this study was an OKO Technologies APO-Q-P500-F8,31 which has square micro-lenses fabricated on fused silica. The

micro-lens array had a 500μm pitch with a focal length of 8.31mm. The array dimensions were 25x25mm resulting in 50 micro-lenses along each dimension [45]. This type of micro-lens array is designed and typically used for wavefront sensing assemblies. The square micro-lenses were advantageous because they closely matched the model developed for the computer simulations. Other light field cameras have been designed using hexagonal micro-lens arrays and alternate designs could be evaluated in future research. The size of the micro-lens array and the focal length of the FZP ensured that the system's FOV was within the FZP limit described by Eq. 5.

A Mikrotron GmbH EoSens® 25CXP camera was used for the detector array and configured with a Nikon 60mm AF-S Micro NIKKOR ED lens to conduct near 1:1 imaging of 1500 grit ground glass placed at the back focal plane of the MLA. As mentioned earlier, the detector array was recessed inside the camera housing, making a relay imaging system necessary. The camera housing was required to help dissipate the heat produced by the sensor, so no attempt was made to remove the detector from the camera housing. The detector array provided excellent resolution, with a total of 5120x5120 sensor pixels. The EoSens® camera used has a monochrome CMOS sensor with a responsivity greater than $1000(V/s)/(W/m^2)$ across the 400nm to 900nm range [46]. Ultimately, the spectral response of the detector limited the spectral range of the system. In this experiment, the detector's range was adequate, but to cover other spectral ranges, a different detector should be used. The MLA, ground glass, and relay imaging system is shown in Fig. 26 to give a better idea of the compact size of the light field camera modification to the imager's back-end detector assembly. This demonstrates how this concept could be easily applied to small satellite payloads or hand held devices.

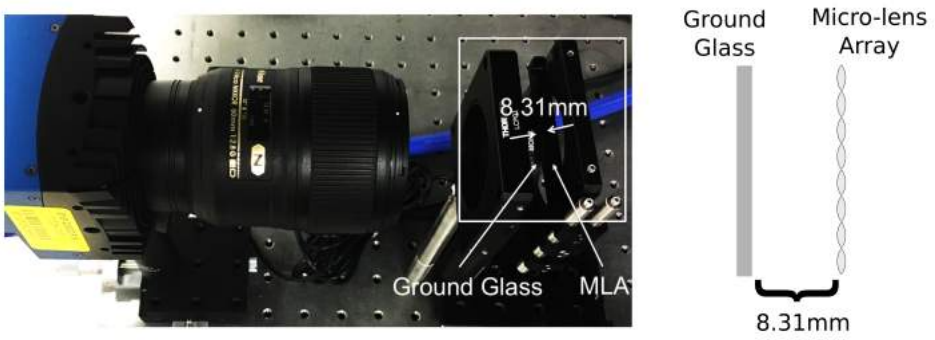

Figure 26. The camera with the SLR lens on the far left images the ground glass that is aligned with the back focal plane of the MLA. The spacing between the ground glass and MLA is only 8.31mm as indicated above. Thus, the light field detection modification to a diffractive optic imaging system has a very small form factor.

4.2 Test Profiles

Light Field PSF Measurement.

The first step in characterizing the performance of the prototype system was measurement of the light field PSF for various wavelengths across the tuning range of the Ti:Sapphire laser. The light field PSF was compared with simulation results to ensure the computational modeling of the system was accurate. In order to conduct the measurements, the rotating diffuser, resolution target and lens L2 were removed from the experimental set-up shown in Fig. 23. Then, the micro-lens array was translated vertically, until the light field PSF was symmetric with respect to the layout of micro-lenses within the array. This adjustment was necessary for the experimental measurements to better visually match the simulation parameters, which assumed point source symmetry with the center micro-lens.

The intensity of the Ti:Sapphire laser and exposure settings of the detector were then adjusted to prevent detector saturation during measurement. The pump power for the Ti:Sapphire laser was set at 8.0W, where the beam quality was known to be excellent, and the beam power was reduced using a reflective ND 3 filter. Additionally, the camera's integration time for a single exposure was set to $1\mu s$.

The exposure settings and reduced laser irradiance were chosen to provide the best visualization of the system's light field PSF at the FZP design wavelength and were adequate for measurement across the full tuning range. At the shorter wavelengths, the output of the laser was reduced as expected. However, the irradiance at the detector was still sufficient to provide a strong detector response at this shorter wavelength, so detector noise factors were insignificant. Following these adjustments, the light field PSF was measured for wavelengths in the 700 to 850nm tuning range of the Ti:Sapphire laser. The wavelengths across the tuning range were selected based on integral increments of the micrometer setting for the Ti:Sapphire's birefringent filter.

Monochromatic Imaging.

After the system's light field PSF for different wavelengths was well characterized, the rotating diffuser, resolution target, and lens L2 were returned to the experimental set-up. This imaging configuration resulted in a much reduced irradiance at the detector plane, so the laser intensity and camera exposure settings were readjusted. This adjustment was again done with the illumination source set at the design wavelength. In order to achieve adequate response at the detector without saturation, the ND 3 filter was no longer required and the camera was set for an integration time of 28ms. These settings were found to provide excellent detector performance for light field collection across the spectral range.

Before collecting light fields to image the resolution target, the micro-lens array was removed from the system to evaluate the baseline chromatic aberration of a conventional camera with a FZP optic. Images of the resolution target were collected across the Ti:Sapphire tuning range as a control group for comparison with the rendered light field images. Then, the MLA was replaced and the light

field was recorded for the same wavelengths. Finally, the resolution target was removed and the light field was collected for the uniformly-illuminated rotating diffuser. This measurement was conducted for calibration of the light field processing algorithms. It identified the positioning and size of the micro-lens images across the detector array at the time of the experimental run which are key parameters for converting the 2-d detector output to a 4-d light field.

Calibration Lamp Spectral Discrimination.

The fundamental characteristic of a spectral imager is its ability to record information in the spectral dimension of an imaged pixel. This basic performance for the prototype system was investigated by collecting the light field formed by two different calibration lamps, then computing the spectral profile for each source. The calibration lamps were shielded to approximate pinhole sources. Additionally, the sources were spatially separated to ensure that spectral crosstalk was not a factor for the computed profiles. The 3-d deconvolution algorithms, where images are rendered based on the spectral light field PSFs, are expected to minimize the influence of out-of-focus components of the signal. On the other hand, spectral crosstalk is expected to significantly effect the performance of digital refocusing techniques.

Another factor that became important for this part of the experiment is the intensity of the calibration lamps. The laser provided a much stronger signal than the calibration lamps. The reduced intensity of these sources required the detector's integration time to be set to a maximum allowed value of 100ms. The reduced signal-to-noise ratio led to a constant offset noise term being significant across the detector array. In order to compensate for this noise, several dark frames were collected, averaged, and subtracted from the collected measurements. This simple control was sufficient to mitigate the noise effects and resolve the spectral profiles of

the collected signals.

V. Results and Analysis

The results of both the simulation and test profiles are discussed in the following sections. The chapter begins by evaluating consistency between simulation and experimental results. Next, monochromatic imaging performance is analyzed. Along with demonstrating refocusing by wavelength, these findings support the possibility of using this type of system for panchromatic imaging with FZP-type optics over larger spectral bands. The spectral sampling characteristics of the FZLFSI are then considered, since this is a fundamental figure of merit for a detector such as this. The chapter closes with a discussion of some potential designs for small satellite sensor payloads and a handheld spectral imaging device.

5.1 Light Field Point Spread Function

The experimentally demonstrated light field PSF for the prototype FZLFSI was seen to closely match the simulation results, as demonstrated in Fig. 27. The measured light field PSF contains noise from the MLA's relay imaging set-up that serves to reduce the effective resolution of the images formed under each micro-lens. However, even with this reduction in quality, the diffraction patterns formed in the individual micro-lens images are seen to be well matched with what is expected. Additionally, the distribution of the light field response across the micro-lens images matches what was predicted. The close agreement between experiment and simulation builds confidence in the accuracy of the computational model and the conclusions drawn from its results.

The light field PSF for this type of camera demonstrates significant differences from traditional plenoptic cameras. In a traditional plenoptic camera, the light field PSF for a focused point is uniform illumination of the full micro-lens image.

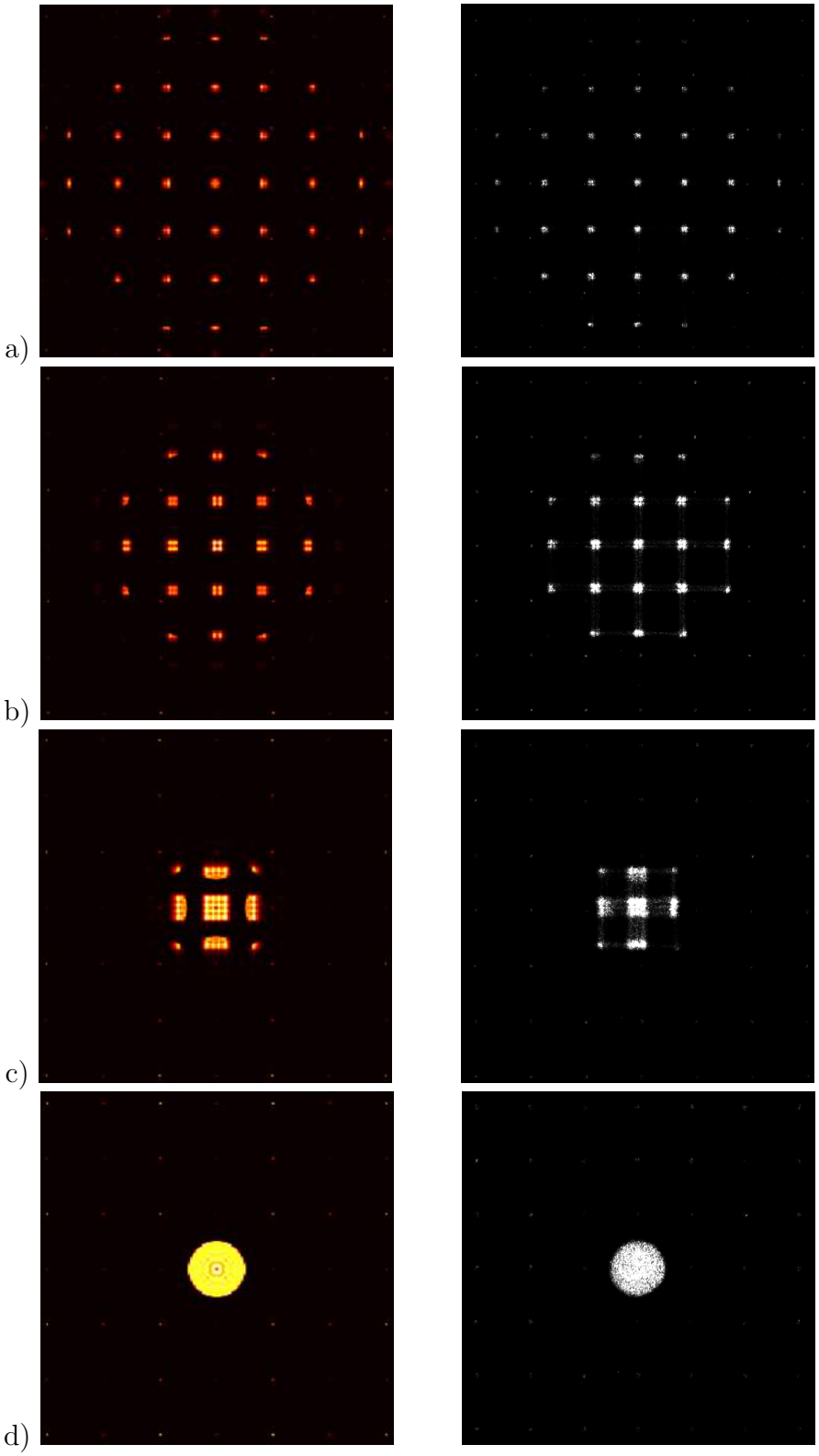

Figure 27. Comparison between (left) simulation results and (right) experimentally measured light field PSFs for a) 716nm, b) 741nm, c) 773nm, and d) 800nm. There is excellent agreement between simulation results and experimental measurements.

However, as seen in the simulation results for 800nm, this is not the case for the FZLFSI. In this type of imager, the micro-lens image is not uniformly illuminated because of the unique structure of the FZP as the objective optic. In principle, each micro-lens images the objective optic at the detector plane. With this understanding, the simulated image under the micro-lens for 800nm agrees with what is expected from the geometrical optics model shown in Fig. 10. There is a dark center to the micro-lens image and the ring structure of the optic is weakly resolved due to the diffraction-limited resolution introduced by the size of the micro-lens aperture. For the unfocused wavelengths, the general shape of the irradiance patterns under the micro-lenses agrees with what is expected by the diffraction effects from a square micro-lens. This diffraction pattern for square micro-lenses has also been demonstrated in similar wave optics simulations for light field microscopes [12].

Another interesting difference from the traditional plenoptic camera is the zeroth order of diffraction, which causes ghost images of the full scene to be formed in the micro-lens images. For example, in Fig. 27 the light field PSF at 800nm has bright spots in the micro-lens images surrounding the center image. The light field PSF for a focused point source is normally a single, uniformly illuminated micro-lens image, without any response elsewhere on the detector. This does not appear to be the case here. A more clear visualization of the effect is achieved by projecting the simulated light field PSF into a 1-d representation in ray-space coordinates. The normalized irradiance profile at the detector is reshaped, such that each column represents a particular micro-lens image. This facilitates better analysis of specific features in the light field response. Figure 28 shows the light field response along the x-dimension for simulated 800 and 600nm light field PSFs. The figure presents an alternate representation of the light field response for 800nm shown in Fig. 27.

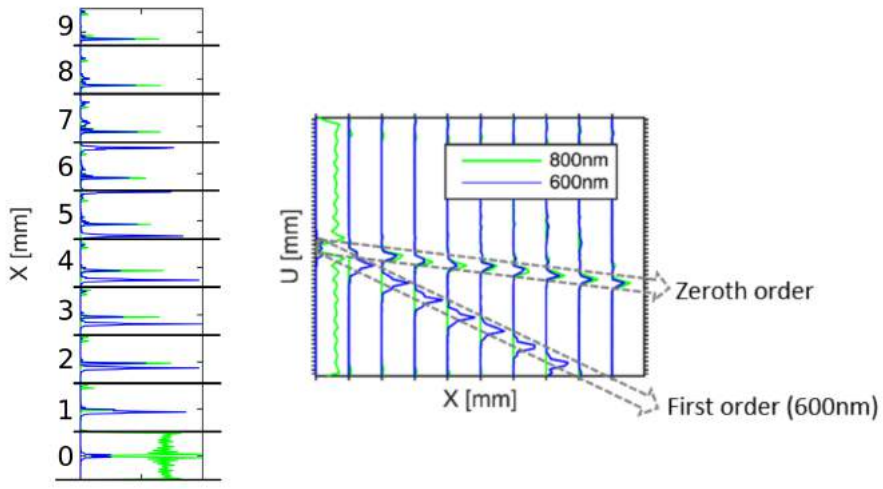

Figure 28. The simulated light field PSF for 800 and 600nm projected to 1-d and translated to ray space coordinates. Each cell of the grid represents a single detector pixel. The blue and green lines indicates the normalized irradiance at each detector pixel across the micro-lens images in the x-dimension and each cell of the grid represents a single pixel of the detector array. The downward shift of the peaks shown for consecutive spatial samples indicates peak formation is shifting towards the center of the array. The peaks near the center of each micro-lens image are independent of wavelength.

The light field response for 600nm is similar to the unfocused wavelengths demonstrated in the same figure. The aligned irradiance peaks from both wavelengths in the micro-lens images adjacent to the center micro-lens image are unique to the FZLFSI. As the location of a particular micro-lens image gets farther away from the center of the MLA, the downward shift in the location of these stray peaks indicates peak formation within the micro-lens image shifts towards the center of the array of micro-lens images for each consecutive image. Also shown in Fig. 28, the location of the peaks in the adjacent micro-lens images remains constant as wavelength is varied. Therefore, these peaks are consistent with what would be expected from the zeroth order. The shifting of peak location within the domain of each micro-lens image is observed based on how the micro-lens images are defined. The domain of each micro-lens image is based on imaging the objective optic. The rays from the zeroth order diffraction of a point source at infinity are

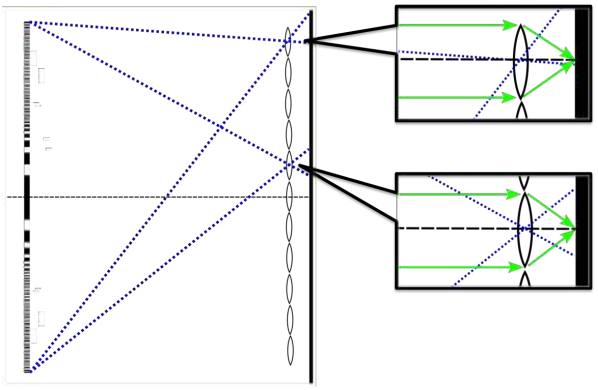

Figure 29. The domain of a micro-lens image is determined by (left) the imaging geometry between the objective optic and a particular micro-lens. The micro-lens images are not formed strictly beneath the physical dimensions of the micro-lenses. On the right, the zeroth order, undiffracted rays, from a point source at infinity are focused to a point aligned with the micro-lens optical axis. Based on how the micro-lens image domain shifts across the array, the formation of the zeroth order focus will shift toward the inner-edge of the micro-lens images for positions far from the center of the array.

imaged to a point aligned with the optical axis of a particular micro-lens, but this point is not necessarily in the center of the micro-lens image which is defined by imaging the FZP as shown in Fig. 29. This effect was consistently observed in the monochromatic synthetic imaging light fields discussed in the next section.

5.2 Monochromatic Synthetic Imaging

The images rendered from the collected light field for monochromatic illumination across the tuning range of the Ti:Sapphire laser achieve the expected resolution of 0.5mm based on the pitch of the MLA (Fig. 30). As discussed in Sec. 2.2, the digital refocusing algorithms used in this thesis are limited to computing images at the resolution of the micro-lens "macro-pixels." Group 0, element 1 of the resolution chart represents a spatial frequency of 1cycle/mm or a line/space width of 0.5mm [47]. Fig. 30 shows that this element is clearly resolved in the refocused images across the tuning range of the Ti:Sapphire laser. For comparison, this same group is barely resolved for imaging with the FZP alone across a maximum spectral

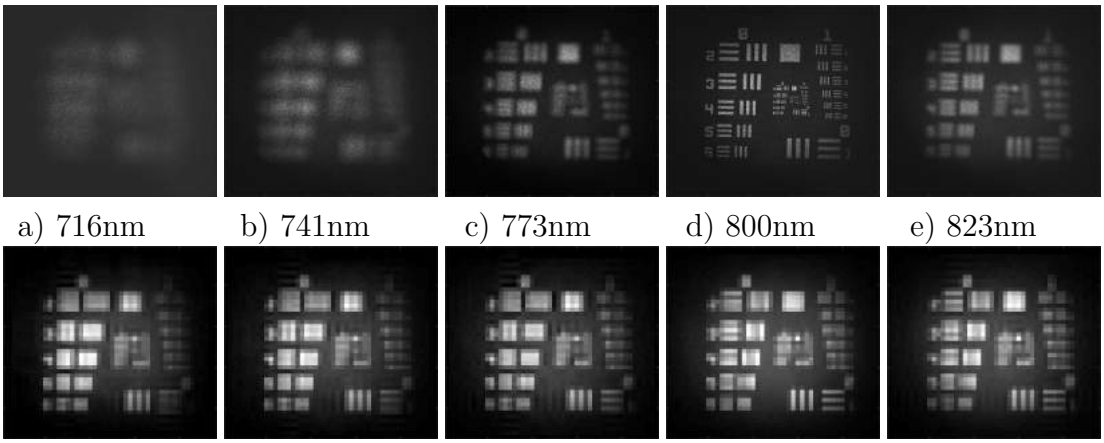

Figure 30. The experimental results for digitally refocused spectral images when illuminated with a tunable Ti:Sapphire laser: The top row shows images formed by a conventional camera with no MLA to collect the light field. The bottom row demonstrates digitally refocused images from processing the collected light field. Group 0, element 1 of the resolution chart is resolved in the digital refocused images across the Ti:Sapphire tuning range. This is the expected resolution that can be obtained from an imager with a 0.5mm pitch MLA.

range of 770 to 820nm.

The design and operation of this type of sensor will be primarily analyzed considering digital refocusing to synthetic image formation planes beyond the design wavelength's focal plane. These longer focal lengths correlate with wavelengths shorter than the FZP design wavelength. As demonstrated by Fig. 30, synthetic imaging is possible for longer wavelengths, but the refocus range will be limited differently by the geometry of the camera. As the synthetic image depth approaches the FZP plane, the focusing performance is no longer well described by the approximations introduced earlier to model FZP behavior.

Beyond the range experimentally demonstrated, an estimate for the full spectral refocusing range can be ascertained from Ng's Fourier analysis of digital refocusing in plenoptic cameras. From this, he showed there is a theoretical limit on computing exact photographs without any loss in resolution. The relation he derives can be

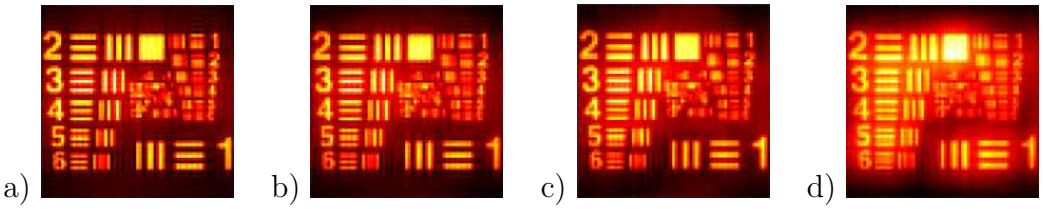

Figure 31. Digitally refocused, simulated monochromatic images of an arbitrarily magnified resolution chart are shown for a) 700nm, b) 600nm, c) 500nm, and d) 400nm. This is the range expected by Eq. 30 for the simulated design, which approximates the effective performance of the prototype system. The rendered images maintain comparable resolutions across the full spectral range.

modified using Eq. 3 to show

$$\lambda_{min} \geq \left[\frac{1}{\lambda_0}\left(1+\frac{\Delta x}{\Delta u}\right)\right] \tag{30}$$

where λ_{min} is the wavelength limitation for perfect digital refocusing, Δx is the spatial sampling rate, and Δu is the angular sampling rate [36]. For the tested prototype, this range is predicted to be larger than the tuning range of the Ti:Sapphire laser. The simulation results shown in Fig. 31 estimate the performance of a system similar to the tested prototype over an extended range. The resolution chart shown in the simulation is arbitrarily magnified to fill the simulated MLA. In

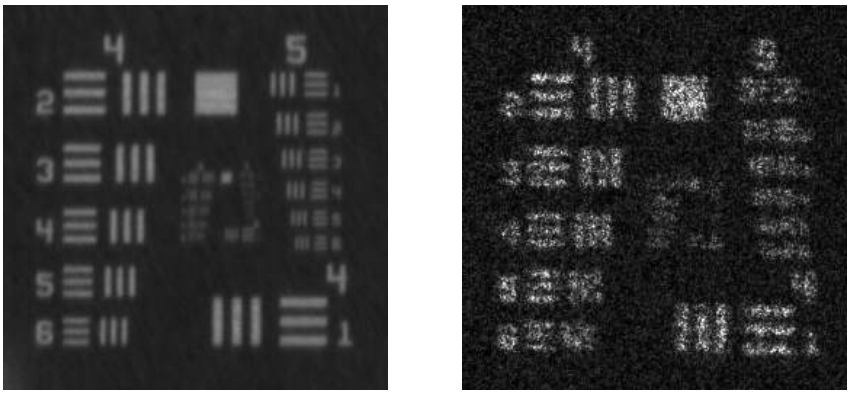

Figure 32. Images of the resolution target produced by the FZP at its design wavelength focused (left) directly onto the detector array and (right) using the relay imaging setup demonstrate the static noise introduced by the ground glass. Comparing the finest well-resolved elements between the two images shows the effective resolution of the relay imaging system is about half the true resolution.

the simulation, the MLA was constructed with 67 micro-lenses in each dimension and 61x61 angular samples per micro-lens image. The experimental configuration had 105x105 angular samples per micro-lens image, but the degraded effective resolution introduced by relay imaging greatly reduced the precision of this sampling.

The relay imaging system reduces the effective resolution of the system by a factor of close to two, as shown in Fig. 32. This means that Δu from Eq. 30 is almost doubled as compared to without the relay imaging system. Therefore, the range predicted by the simulation will be close to that of the experimentally demonstrated system. This equates to an expected lower limit for the prototype system around 400nm for exact digital refocusing. Beyond this range, refocusing will still be possible with reduced image quality [36]. The angular sampling rate in the experiment was not limited by the size of detector pixels, but instead by the static noise introduced by the ground glass in the relay imaging system. Even with degraded angular resolution, the prototype system demonstrated excellent performance across the spectral range of the Ti:Sapphire laser, as expected. An imager constructed without the relay imaging set-up is expected to achieve a much improved spectral range.

During experimental measurement of the light fields used for digital refocusing, images of the full object were observed in the micro-lens images as discussed in the previous section (Fig. 33). The dynamic range of the sensor for the experimentally measured light field obscures this effect in the fully illuminated micro-lens images. However, the effect is clearly demonstrated in the darker micro-lens images. The formation of these ghost images of the object is also demonstrated in Fig. 19. These images are observed in the other measured and simulated micro-lens images throughout this paper. The zeroth-order images do not appear to affect the

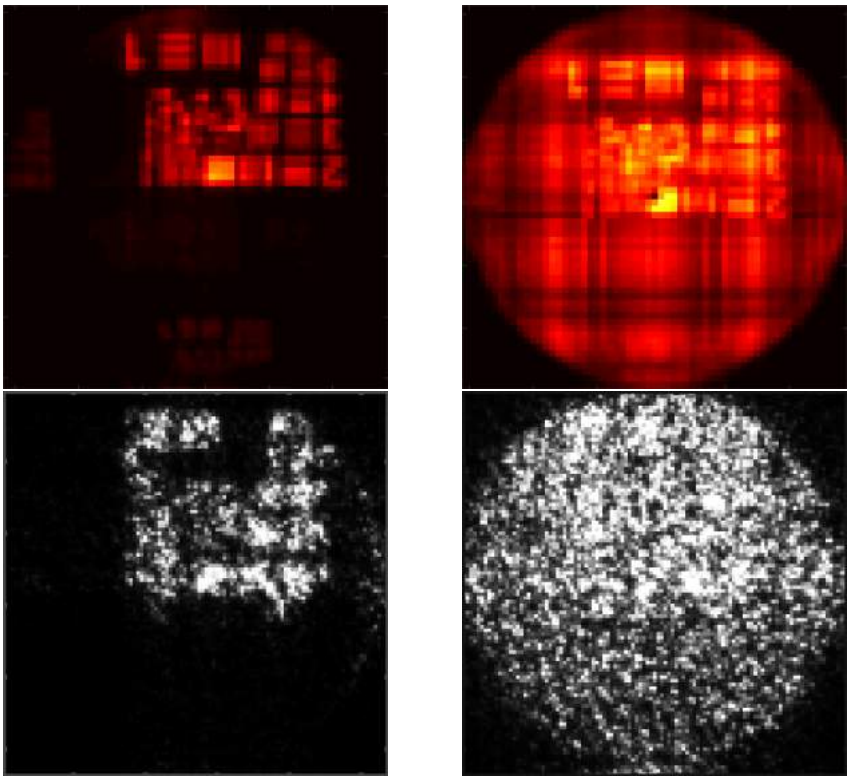

Figure 33. Ghost images of the entire object from the zeroth order of diffraction form in each micro-lens image. The left column shows what would normally be dark micro-lens images due to the light field effect, and the right column shows fully illuminated images. (top) Simulated micro-lens images are shown along with (bottom) experimentally measured. For the fully illuminated micro-lens image from the experiment, the ghost image is difficult to resolve because of the computational precision of the measured image.

performance of the light field camera. More detailed investigation of this effect could be considered for future study in order to better understand the potential advantages and disadvantages of this phenomenon.

5.3 Spectral Sampling

In Sec. 3.1, the geometrical limitations on the spectral resolution of this system were introduced and close to a 15nm spectral sampling limit was predicted. This limit is based on the minimum spectral variation required for significant change to the measured light field PSF. These changes in the light field PSF are only well

detected using 3-d deconvolution methods to process the collected light field. As a result, the traditional digital refocusing methods can only be used as an estimate for the spectral sampling performance of the system. Similarly, the degree of uncertainty in computing object depth from digital refocusing has been investigated in previous studies [9]. The traditional refocusing methods also do not account for the out-of-focus contributions from adjacent spectral bins. This study measured the spectral profiles of two well spatially separated sources to demonstrate the fundamental capability of this type of detector. The results are shown in Fig. 34. The digital refocusing algorithm was computed for the synthetic image plane depth of each spectral bin to build a spectral data cube. Then the irradiance of the rendered pixel corresponding to a particular lamp was plotted against wavelength. While using the digital refocusing algorithms did not recover much of the spectral structure of the two sources, it was able to clearly distinguish between the unique spectral profiles of the calibration lamps. The prototype is clearly capable of identifying the different spectral structures of pixels within a rendered image.

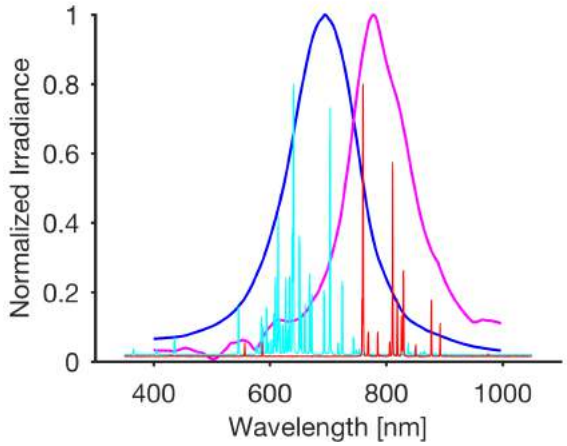

Figure 34. Irradiance of the rendered pixels correlated to the Hg-Ne (blue) and Kr (violet) calibration lamps from digitally refocused photographs at the synthetic imaging depth for wavelengths across the spectral range. The two sources were well-separated during measurement to ensure spectral cross-talk was not a factor when computing the shown profiles. These computed spectral profiles are compared with the higher resolution spectra recorded by the spectrometer for Hg-Ne (cyan) and Kr (red).

However, this also demonstrates the limited utility of using the digital refocusing algorithms for processing the spectral dimension of the light field. In order to better recover the spectral structure of the signal, 3-d deconvolution methods should be applied.

The full complexity of performing a spectral 3-d deconvolution for this system was not approached, and the scope was limited to constructing the spectral structure for a single, isolated pixel. As discussed in Sec. 3.2, a Richardson-Lucy iteration is one approach to forming the most likely estimate of the true spectral data cube. This method was implemented on the light fields measured for the Hg-Ne calibration lamp. The Richardson-Lucy iteration was performed for spectral bins sampled every 15nm. The light field PSF used in the Richardson-Lucy iterations for each spectral bin was computed by the wave optics model. The results of the simulation were then scaled to match the resolution of the experimentally collected light fields. The close agreement between the simulation and experimental measurements demonstrated in Fig. 27 shows that this implementation should provide accurate results. As a result, Fig. 35 shows that much of the spectral structure could be recovered through implementation of 3-d deconvolution methods. There appear to be some artifacts in the computed spectral structure and this thesis does not robustly evaluate the performance of this processing algorithm. Further development and optimization of these techniques is needed to efficiently compute accurate spectral data cubes from the collected light fields.

Additional testing was done to investigate the level of spectral cross-talk between pixels in the rendered image. The blurred contributions from the out-of-focus spectral components of nearby pixels will influence the computed spectrum for the pixel of interest. This cross-talk will cause erroneous spectral peaks to be present in the computed spectral profile. It was found to become significant for rendered pixel

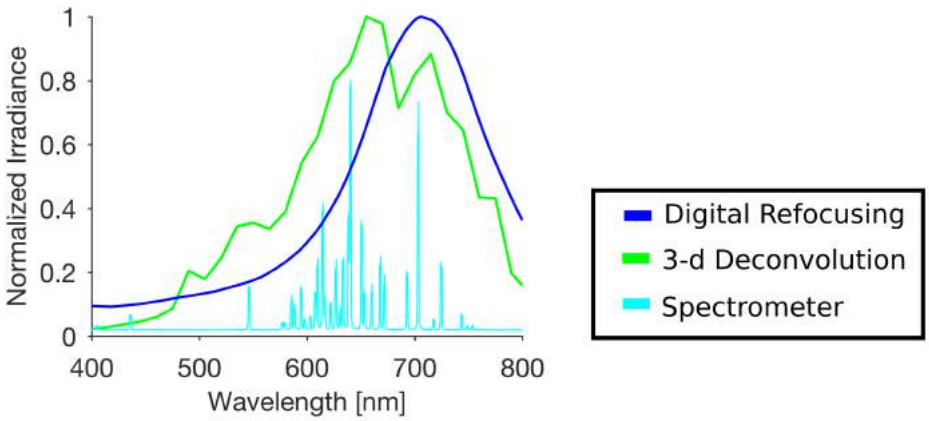

Figure 35. Compares the irradiance of the Hg-Ne calibration lamp for each spectral bin computed using a 3-d deconvolution method (green) and a digital refocusing algorithm (blue). For reference, (cyan) shows the spectra measured by a spectrometer. The 3-d deconvolution method is clearly superior for resolving specific features of the spectral profile.

separations less than three, as shown in Fig. 36. These measurements were conducted by creating a monochromatic point source, from the focused Ti:Sapphire beam, very close to the calibration lamp aperture. When the two sources were separated by less than three pixels, spectral cross-talk became a significant factor when computing the spectral profile of the calibration lamp. As mentioned earlier, 3-d deconvolution methods are expected to minimize this cross-talk. Figure 37 compares the computed spectral profile from digital refocusing to that obtained from the Richardson-Lucy method. This figure clearly demonstrates the utility of the 3-d deconvolution processing techniques for computing the spectral dimension.

As an imaging spectrometer, an important figure of merit for this system is its spectral sampling performance. This performance can be broken down into two characteristics, spectral range and resolution. The highest achievable spectral resolution is ultimately limited by the FZP, but the MLA and detector array determine how finely the spectrum can be computationally sampled using this system. This is similar to the depth discrimination properties of traditional plenoptic camera designs. In these designs, depth discrimination is most

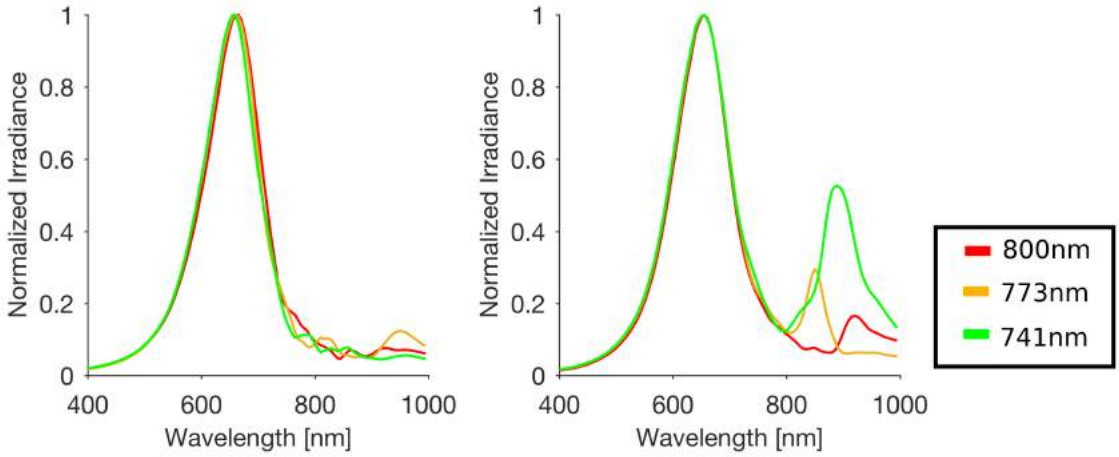

Figure 36. The Hg-Ne calibration lamp and a point source created by focusing a portion the collimated beam from the Ti:Sapphire were placed close together in the object plane to evaluate the level of spectral cross-talk between rendered image pixels. The computed Hg-Ne spectral profile is shown for nearby point sources at 800nm (red), 773nm (orange), and 741nm (green). The rendered pixels for each source were separated by 3 pixels (left) and 2.8 pixels (right). At separations less than 3 pixels, erroneous spectral peaks significantly modify the computed spectral profile for the pixel of interest.

significantly improved through increased spatial sampling, which means, smaller micro-lens widths [9, 48]. The smaller micro-lenses increase spatial sampling at the cost of angular sampling because there are fewer pixels per micro-lens image. This

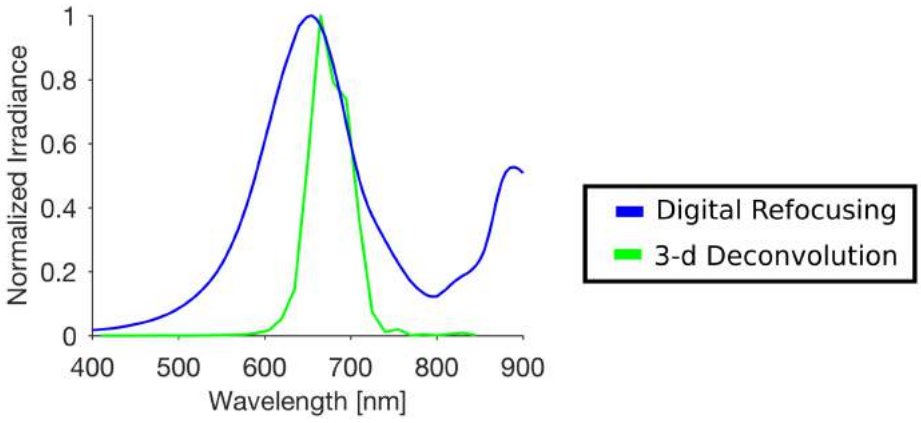

Figure 37. The computed spectral profiles of the Hg-Ne calibration lamp with a nearby point source at 741nm are compared between digital refocusing (blue) and Richardson-Lucy deconvolution (green) methods. Spectral cross-talk is not observed for the 3-d deconvolution technique.

reduction in the angular sampling rate limits the spectral range of the device as discussed in Sec. 2.2.

The maximum achievable spectral sampling rate of the simulated system was previously estimated based solely on geometrical optics. This resolution is better demonstrated across the spectral range by using the wave optics model to evaluate the minimum change in wavelength that produces distinct features within the two wavelengths' light field PSFs. The irradiance of any real signal is not expected to be uniform across a spectral band, and any overlapping features would not be well resolved. Therefore, the size of the spectral bins sampled by this device will depend on the formation of unique spectral light field PSFs. Wave optics simulations of the

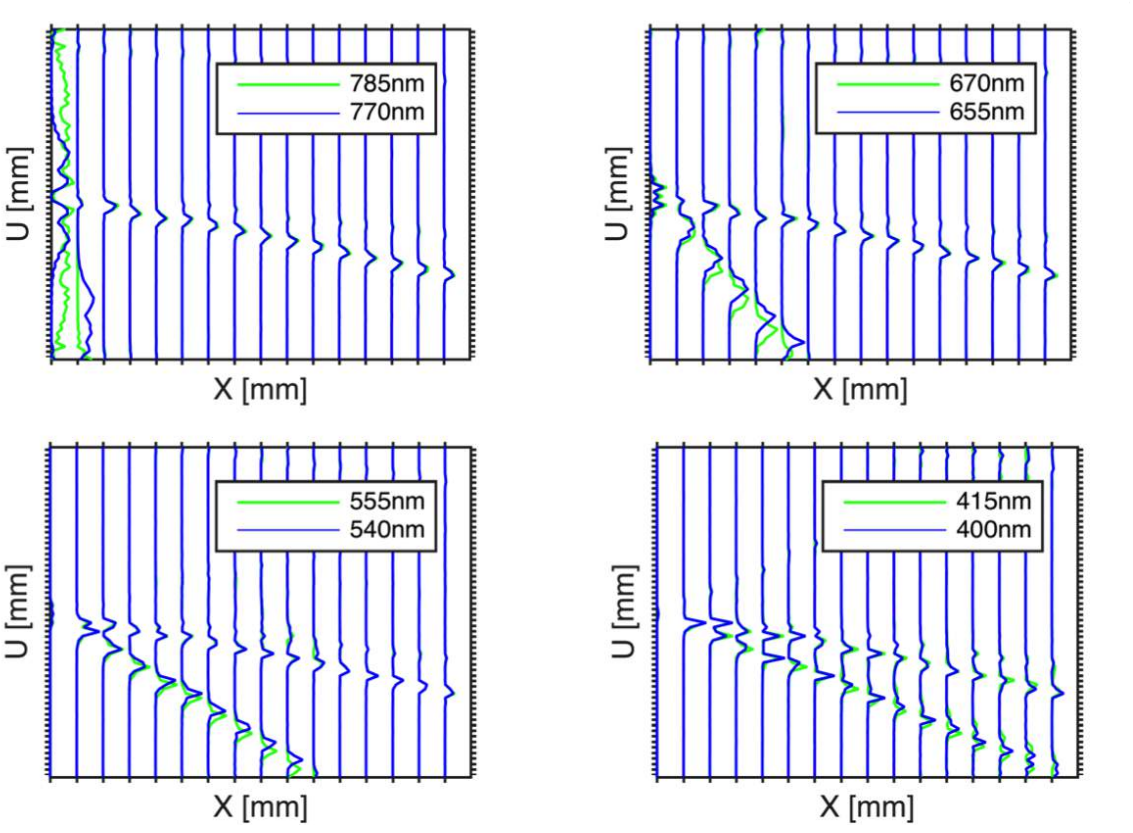

Figure 38. 1-d ray space projection of the simulated light field are shown for various wavelengths across the sensor's spectral range. The tick marks indicate the pixels within each micro-lens image. A 15nm wavelength separation in each of these spectral regions maintains distinct features in the light field PSFs down to 400nm. This sampling rate defines the size of the spectral bins measured by the system.

prototype system confirm the geometrical model's estimate for 15nm spectral bins as demonstrated in Fig. 38.

The simulation results from Fig. 38 indicate that a 15nm sampling rate is possible down to 400nm. For a signal that includes noise and intensity variation across the spectral band, this sampling rate may cause difficulties near 400nm because of the degree of similarity between the demonstrated spectral light field PSFs. This shows that the digital refocusing limit described in Eq. 30 is close to where the spectral sampling rate becomes inadequate. The digital refocusing limit will be used to analyze the spectral range of the proposed system designs presented in the next section.

5.4 Design Optimization

The prototype system demonstrated in this thesis is certainly not an optimized design. The prototype was built to validate the concept and provide a baseline for further improvement. Future studies should provide more comprehensive characterization of FZLFSI systems designed to suit specific applications. This section will discuss the optical design considerations identified in this study that determine the spatial and spectral sampling characteristics for this type of system. It is worthwhile to note that a key figure of merit not characterized in this study that will significantly affect system performance is radiometric sensitivity. Characterizing the radiometric sensitivity becomes more appropriate once a system is designed for a particular application. There will inevitably be a trade-off between the spectral sampling performance of the system and radiometric sensitivity.

These two aspects of performance are directly related to the detector assembly. A design optimization scheme should begin with considering the detector array since this component will be the key limiting factor because it directly determines the

lower limit for micro-lens size. As shown previously, the pitch of the detector array compared to the MLA determines the degree of angular sampling provided by the imager. The angular sampling rate determines the spectral range for a given micro-lens as described by Eq. 30 and is a fundamental aspect of all light field imaging systems. The pitch of the detector array is a key factor limiting the minimum size of the micro-lenses. Also, the size of individual sensor elements in the detector array directly influences the radiometric sensitivity of the system. There will be a limit to the minimum size of detector pixels that still provides adequate response for the expected spectral radiance values associated with a chosen application. Selecting a detector array requires balancing the radiometric sensitivity of the detector against the desired spectral range of the device.

Once a detector array is chosen, the next step will be the design of the MLA. As seen in the previous results, micro-lens size determines both spectral and spatial resolution. Due to the axial dispersion property of the system, optimization of spectral resolution will also maximize spatial resolution. For this portion of the design, the important trade-off is between spectral resolution and range. The spectral range is described by Eq. 30 and the resolution by Eq. 10. The prototype system demonstrated a maximum spectral resolution of 15nm over a range from 800 to 400nm. The spatial resolution of the system can then be determined based on the width of the micro-lenses and design focal length. For the prototype demonstrated, the micro-lens size and system f/# correspond to an instantaneous FOV (IFOV) of 0.36 radians. The demonstrated IFOV is certainly adequate for certain applications, but the rendered image resolution of 50x50 is low. These limitations in the prototype system could be easily improved with finer MLA pitch and an array size that uses the full FOV provided by the FZP. To give an idea of the space for improvement, the micro-lenses used in this study are almost 40 times

larger than those used in some commercially available plenoptic cameras. As an example of how the spectral range decreases and spatial resolution increases with reduced micro-lens size, Fig. 39 compares the performance of similar optical systems with 500, 200, and 100μm micro-lenses. Additionally, the spectral resolution is expected to increase, as shown in Fig. 40.

The light field detector design was the dominant effect that limited the spectral resolution of the systems demonstrated in this thesis. However, as designs seek to achieve the highest possible spectral resolution, the spectral response of the FZP may become significant. The design parameter that sets the spectral resolution of the FZP is the f/# of the system. Low FZP f/# was shown to narrow the spectral

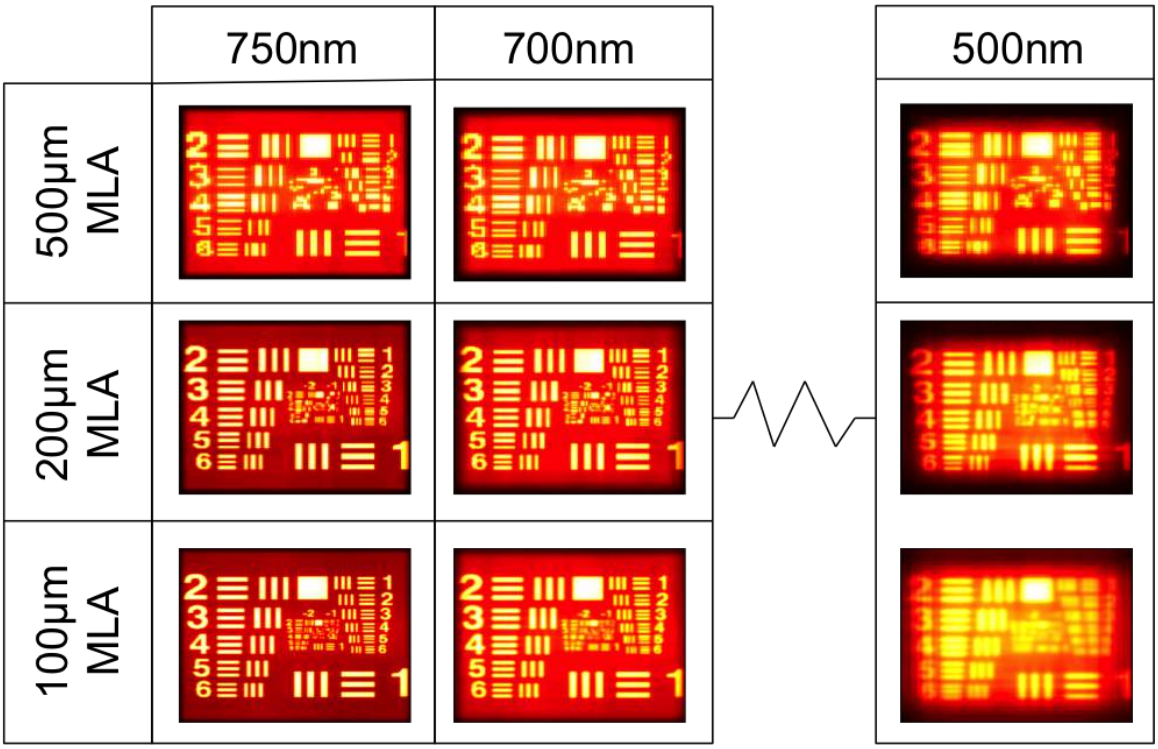

Figure 39. The spectral range to achieve exact digital refocusing performance is compared between different designs for 500, 200, and 100μm micro-lenses. The modeled systems use the same 30mm FZP designed for 800nm and similar sampling rates at the detector plane. The rendered image's spatial resolution for the smaller micro-lenses is clearly superior, but the spectral range is reduced. The predicted spectral ranges for each design from Eq. 30 are approximately 400, 100, and 40nm, respectively.

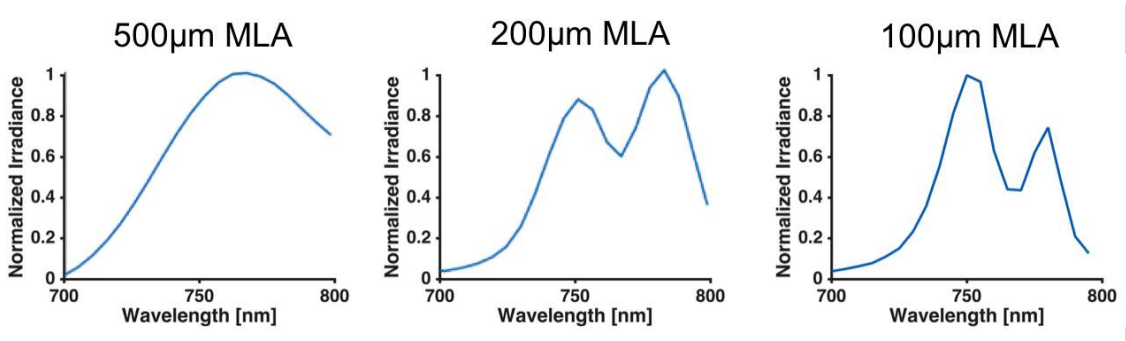

Figure 40. Spectral resolution is compared between systems designed with 500, 200, and 100μm micro-lenses. The modeled systems use the same 30mm FZP designed for 800nm and similar pixel sizes at the detector plane. The spectral profiles were computed for a single point source emitting at 750 and 780nm. The digital refocusing method demonstrates how spectral resolution improves with reduced micro-lens size. However, it does not accurately reflect the maximum achievable spectral resolution.

depth of focus and is desired, similar to how lower f/# increases depth discrimination in standard plenoptic cameras [48]. This will only be significant if the spectral sampling rate described by Eq. 10 approaches the spectral resolution of the FZP.

Proposed Designs for Future Systems.

Based on the previous discussion, three system designs are presented to better describe some of the potential capabilities of this type of sensor (Table 1). First, a panchromatic imaging payload for a small satellite could be built using a photon

	Panchromatic	NIR spectral imager	Handheld device
FZP diameter (mm)	200	100	30
Micro-lens diameter (μm)	14	470	100
Detector pixel size (μm)	1.7	4.5	1.7
Spectral bin width (nm)	0.046	5.64	2.67
Spectral range (nm)	0.378	395	131
IFOV(mrad)	0.125	2.35	1.67

Table 1. Proposed system design schemes for potential application of this type of sensor. The first two systems are designs proposed as sensor payloads for small satellites. The third scheme presents the capabilities of a handheld, small form factor snapshot spectral imager. All of the proposed designs are f/2 systems.

sieve as the objective optic. Falconsat-7 is a 3U CubeSat configured with a 200mm membrane photon sieve designed to conduct solar imaging at a wavelength of 656.45nm (H-alpha). The optical subsystem currently requires a narrowband, 0.7 angstroms FWHM, H-alpha filter to eliminate out-of-focus spectral contributions near the desired wavelength [17]. A FZLFSI could be designed using the same objective optic design with a 14μm MLA and a detector array with 1.7μm pixels. As shown in the table, this would provide a 3.78 angstroms spectral range for generating perfectly refocused panchromatic images. This is certainly an improvement in the spectral bandwidth of the detector as compared to using the filter but would also result in decreased spatial resolution. The reduced resolution is about one eighth of the diffraction limited resolution the system could achieve without the light field detector modification. This spatial resolution could be improved with a corresponding reduction in spectral range, which ultimately will be limited by the fabrication limits on the pitch of the micro-lens and detector arrays.

The second example is a NIR spectral imager that could be constructed as a small satellite sensor payload. This design has a much broader spectral range at the cost of reduced spatial and spectral resolution. This represents the fundamental design trade-off for this type of system. Increased spectral range reduces spectral and spatial sampling rates.

The last proposed system is a compact, handheld spectral imaging concept. This demonstrates a more balanced design between spectral range and resolution. An application for the handheld imager would be for the detection and investigation of specific material signatures in an area of interest. The handheld imager would be designed for a spectral region containing unique spectral features of the target material. Alternatively, a design of this type could detect disturbed earth signatures for counter improvised explosive device (C-IED) purposes. Areas with disturbed soil

have been shown to demonstrate detectable changes in the quartz Reststrahlen band [49]. The Reststrahlen band is a relatively narrow spectral region that this type of sensor could interrogate at a high spectral sampling rate. This would provide the troops on the ground with an on-scene tool to identify hazard areas and opens up possibilities for redundant identification of threats across multiple modalities.

These proposed designs represent a small subset of all the possible applications of this sensor. Another key advantage of this sensor not discussed above is that the entire spectral profile is captured in a single snapshot, and thus, it may provide substantial capability for spectral imaging of dynamic environments like gas plumes.

VI. Conclusion

6.1 Contributions

This study has demonstrated the Fresnel zone light field spectral (FZLFSI) concept, showing that it can be used to distinguish between spectrally unique points in an image. The prototype system was also able to render digitally refocused images, based on wavelength, across a range of more than 100nm. This experimentally demonstrated performance shows the potential capabilities of FZLFSI systems and sets the foundation for further development. This work also provides a computational model that accurately simulates the performance of this type of system. Particular designs will inevitably be linked to operational requirements, and the computational model can be used to evaluate the performance of the optical system with varied design parameters. This thesis consolidates the key Fresnel zone plate and light field camera design trade-offs to better inform the development of future systems. Since the scope of this thesis was limited to demonstration of the system and basic characterization of optical performance, there are significant opportunities for future work to further evolve this concept as discussed in the next section.

6.2 Future Work

The prototype system demonstrated in this thesis is far removed from an optimized design of this type of imager for any application. Further research into design optimization will better refine the range of unique capabilities offered by this system. Improved designs will provide much better spectral and spatial resolution balanced against the desired spectral range of operation. These particular designs and the associated design trade-offs should be further evaluated for generalized light

field camera designs. For example, a system based on a focused plenoptic camera light field detector configuration would offer much better spatial resolution with some reduction in angular sampling and thus spectral range. This type of design may be better suited for rendering panchromatic, extended spectral depth of field images. Additionally, future systems should be designed with photon sieves as the objective optic. The photon sieve is a more realistic option for operational employment of this system.

Another goal for future research should be characterization of this type of system's radiometric sensitivity. As part of this, the noise equivalent spectral radiance (NESR) limits for a detector are a key factor to determine suitable operational employments of the sensor. NESR should be evaluated for this system, especially because binary diffractive optics will inherently limit the detection efficiency for weak signals. Additionally, further study should be done on spectral calibration methods for a FZLFSI. When dealing with weak signals, detector offset and gain noise factors becomes significant. Consistent spectral performance for varied signal strengths requires robust spectral calibration of the detector.

Design optimization and radiometric sensitivity characterization would also both benefit from an improved computational model of the FZLFSI. The simulation has difficulty modeling FZP structures with many rings because the sampling criteria discussed earlier. Huge arrays are needed to fully sample the structure of the outermost rings. As these rings become smaller, finer sampling is required. The model also does not include any noise factors and converting it to a stochastic model would aid with fundamental characterization of the radiometric sensitivity. A simulation that includes modeling of noise factors would help inform future system designs to support applications where weaker signals are expected.

Finally, in order to exploit the full spectral imaging capability of this system,

robust and efficient 3-d deconvolution methods are needed. The implementation of these methods will minimize spectral cross-talk between pixels and maximize the achievable spectral resolution for the system. Computational methods are crucial for light field processing and maximizing the performance of light field sensors. The 3-d deconvolution method proposed in this thesis was based on findings from light field microscopy research. Future studies should consider the full range of light field computational methods to provide a better implementation for processing the light fields collected by a FZLFSI.

6.3 Closing Remarks

There is considerable potential for future FZLFSI systems that will offer unique capabilities to both the spectral imaging and binary diffractive optic research communities. Not only does this type of system provide a compact snapshot spectral imaging capability, but it also could expand the bandwidth of photon sieve panchromatic imaging systems. While the demonstrated spatial resolution was relatively low, future designs can easily achieve improved performance. This type of system provides a simple, compact optical design of a spectral imager that could be optimized for a variety of applications. Given current manufacturing standards for all the components involved in this type of system, it is feasible to construct a high resolution, snapshot spectral imager. Additionally, the demonstrated concept provides a new possibility for broadband panchromatic imaging with diffractive optics such as the photon sieve. The spatial resolution of such a device would be limited by the pitch of the micro-lens array but would still provide a significant new capability. Furthermore, resolution limitations may be minimized in future designs based on generalized plenoptic camera designs where the micro-lens array is not necessarily positioned at the design focal length. There is significant trade-space for

the different components in a FZLFSI design and this project has established baseline characteristics to help evolve future designs. There is still significant work to be done to optimize FZLFSI design to support relevant operational sensing requirements and fully realize the unique capabilities offered by this type of detector.

Bibliography

1. O. E. Myers, "Studies of transmission zone plates," *Am. J. Phys.*, vol. 19, no. 6, pp. 359–365, 1951.

2. Q. Cao and J. Jahns, "Comprehensive focusing analysis of various Fresnel zone plates," *J. Opt. Soc. Am. A*, vol. 21, no. 4, pp. 561–571, 2004.

3. M. Young, "Zone plates and their aberrations," *J. Opt. Soc. Am.*, vol. 62, no. 8, pp. 972–976, 1972.

4. C. M. Tulip, "Photon Sieve Bandwidth Broadening by Reduction of Chromatic Aberration Effects Using Second-Stage Diffractive Optics," Master's thesis, Air Force Institute of Technology, 2015.

5. S. J. Myers, "Design, Analysis, and Characterization of an Optical Photon Sieve for Space-Based Imaging Systems," Master's thesis, Air Force Institute of Technology, 2014.

6. F. S. Oktem, F. Kamalabadi, and J. M. Davila, "High-Resolution Computational Spectral Imaging with Photon Sieves," in *IEEE International Conference on Image Processing (ICIP)*. IEEE, 2014, pp. 5122–5126.

7. M. Hinnrichs and M. Massie, "New approach to imaging spectroscopy using diffractive optics," *Proc. of SPIE*, vol. 3118, pp. 194–205, 1997.

8. Z. Zhou and B. Xiangli, "Snapshot Multispectral Imaging using a Plenoptic Camera with an Axial Dispersion Lens," in *Computational Optical Sensing and Imaging*. Optical Society of America, 2014, pp. CTu2C–4.

9. R. A. Raynor, "Rangefinding with a Plenoptic Camera," Master's thesis, Air Force Institute of Technology, 2014.

10. R. Ng, M. Levoy, M. Bredif, G. Duval, M. Horowitz, and P. Hanrahan, "Light field photography with a hand-held plenoptic camera," *Computer Science Technical Report CSTR*, vol. 2, no. 11, pp. 1–11, 2005.

11. R. Ng, "Digital Light Field Photography," Ph.D. dissertation, Stanford University, 2006.

12. M. Broxton, L. Grosenick, S. Yang, N. Cohen, A. Andalman, K. Deisseroth, and M. Levoy, "Wave optics theory and 3-D deconvolution for the light field microscope," *Opt. Express*, vol. 21, no. 21, pp. 25 418–25 439, 2013.

13. W. W. Hu, K. Sarveswaran, M. Lieberman, and G. H. Bernstein, "Sub-10 nm electron beam lithography using cold development of poly(methylmethacrylate)," *Journal of Vacuum Science & Technology, B:*

Microelectronics and Nanometer Structures Processing, Measurement, and Phenomena, vol. 22, no. 4, pp. 1711–1716, 2004.

14. Q. Cao and J. Jahns, "Modified Fresnel zone plates that produce sharp Gaussian focal spots," *J. Opt. Soc. Am. A*, vol. 20, no. 8, pp. 1576–1581, 2003.

15. L. Kipp, "Sharper imaging by focusing soft X-Ray with photon sieves," *Nature*, vol. 414, no. 6860, pp. 184–188, 2001.

16. G. Andersen, "Large optical photon sieve," *Optics letters*, vol. 30, no. 22, pp. 2976–2978, 2005.

17. O. Asmolova, G. Andersen, M. G. McHarg, T. Quiller, C. Maldonado, and T. Dickinson, "Design and test of a novel solar imaging payload for small satellites," *Proc. of SPIE*, vol. 9602, 2015.

18. A. Lumsdaine and T. Georgiev, "Full Resolution Lightfield Rendering," Indiana University and Adobe Systems, Tech. Rep., 2008.

19. Y. Park, L. Koch, K. D. Song, S. Park, G. King, and S. Choi, "Miniaturization of a Fresnel spectrometer," *J. Opt. A: Pure Appl. Opt.*, vol. 10, no. 9, p. 095301, 2008.

20. E. H. Adelson and J. Y. Wang, "Single lens stereo with a plenoptic camera," *IEEE transactions on pattern analysis and machine intelligence*, vol. 14, no. 2, pp. 99–106, 1992.

21. T. Georgiev, K. C. Zheng, B. Curless, D. Salesin, S. Nayar, and C. Intwala, "Spatio-Angular Resolution Tradeoffs in Integral Photography," *Rendering Techniques*, vol. 2006, pp. 263–272, 2006.

22. E. Hecht, *Optics - 4th ed.* Addison Wesley, 2002.

23. S. Frank L. Pedrotti and L. S. Pedrotti, *Introduction to Optics.* Upper Saddle River, New Jersey: Prentice Hall, 1993.

24. T. W. N. Dickinson, "Simulation, design, and test of square, apodized photon sieves for high-contrast, exoplanet imaging," Master's thesis, Air Force Institute of Technology, 2016.

25. A. Boivin, "On the theory of diffraction by concentric arrays of ring-shaped apertures," *J. Opt. Soc. Am.*, vol. 42, no. 1, pp. 60–64, 1952.

26. M. Sussman, "Elementary diffraction theory of zone plates," *Am. J. Phys.*, vol. 28, no. 4, pp. 394–398, 1960.

27. A. Lumsdaine and T. Georgiev, "The focused plenoptic camera," in *Computational Photography (ICCP), 2009 IEEE International Conference on*, 2009, pp. 1–8.

28. E. L. Dereniak and G. D. Boreman, *Infrared Detectors and Systems*. Wiley-Interscience, 1996.

29. J. P. Anglin, "3D Volume Reconstruction from 2D Plenoptic Data using FFT-based Methods," Ph.D. dissertation, Auburn University, 2015.

30. P. Anglin, S. J. Reeves, and B. S. Thurow, "Characterization of Plenoptic Imaging Systems and Efficient Volume Estimation from Plenoptic Data," *AUrora, Auburn University*, 2015. [Online]. Available: http://hdl.handle.net/11200/48467

31. J. T. Verdeyen, *Laser Electronics*, 3rd ed., J. Nick Holonyak, Ed. Prentice Hall, 1995.

32. J. W. Goodman, *Introduction to Fourier Optics, 3d ed.* Roberts and Company, 2005.

33. S. A. Shroff and K. Berkner, "Image formation analysis and high resolution image reconstruction for plenoptic imaging systems," *Applied Optics*, vol. 52, no. 10, pp. D22–D31, 2013.

34. J. D. Schmidt, *Numerical Simulation of Optical Wave Propagation in MATLAB*. Bellingham, WA: Society of Photo-Optical Instrumentation Engineers, 2010.

35. D. Voelz, *Computational Fourier Optics: A MATLAB Tutorial*. Bellingham, WA: Society of Photo-Optical Instrumentation Engineers, 2011.

36. R. Ng, "Fourier slice photography," in *ACM Transactions on Graphics (TOG)*, vol. 24, no. 3. ACM, 2005, pp. 735–744.

37. T. Georgiev. (2010, February) Computational methods for radiance. Adobe Systems Inc. [Online]. Available: www.tgeorgiev.net/EG10/Computation.pdf

38. *Model 3900S CW Ti:Sapphire User's Manual*, Spectra-Physics, Mountain View, CA, 2002.

39. *Exemplar Smart CCD Spectrometer Datasheet*, B & W Tek, Inc., 19 Shea Way, Newark, DE, 2015.

40. W. J. Smith, *Modern Optical Engineering*, 4th ed. McGraw-Hill, 2008.

41. *Typical spectra of spectral calibration lamps*, Oriel Instruments, Stratford, CT U.S.A.

42. T. Stone and N. George, "Hybrid diffractive-refractive lenses and achromats," *Applied Optics*, vol. 27, no. 14, pp. 2960–2971, 1988.

43. P. Valley, "Flat Liquid Crystal Diffractive Lenses with Variable Focus and Magnification," Ph.D. dissertation, The University of Arizona, 2010.

44. T. Togino and M. Nakaoka, "Optical system and image display apparatus," Jan. 30 2001, uS Patent 6,181,475. [Online]. Available: https://www.google.com/patents/US6181475

45. *OKO Guide to Adaptive Optics*, 4th ed., OKO Technologies, Polakweg 10-11, 2288 GG, Rijswijk ZH, The Netherlands, May 2013.

46. *EoSens 25CXP Reference Guide*, Mikrotron GmbH, Landshuter Str. 20-22, 85716 Unterschliessheim, Germany, 2015.

47. *T-20 USAF 1951 Chart Standard Layout Product Specifications*, Applied Image Inc., Rochester, NY U.S.A.

48. V. Drazic, J.-J. Sacre, A. Schubert, J. Bertrand, and E. Blonde, "Optimal design and critical analysis of a high-resolution video plenoptic demonstrator," *Journal of Electronic Imaging*, vol. 21, no. 1, pp. 011 007–1, 2012.

49. M. Cathcart, A. Thomas, T. Harrell, and S. Lane, "Final Report Army Advanced Concept Workshop on Disturbed Soil Characterization and Exploitation," *GTRI Report*, vol. 30, 2008.

REPORT DOCUMENTATION PAGE

Form Approved
OMB No. 0704–0188

The public reporting burden for this collection of information is estimated to average 1 hour per response, including the time for reviewing instructions, searching existing data sources, gathering and maintaining the data needed, and completing and reviewing the collection of information. Send comments regarding this burden estimate or any other aspect of this collection of information, including suggestions for reducing this burden to Department of Defense, Washington Headquarters Services, Directorate for Information Operations and Reports (0704–0188), 1215 Jefferson Davis Highway, Suite 1204, Arlington, VA 22202–4302. Respondents should be aware that notwithstanding any other provision of law, no person shall be subject to any penalty for failing to comply with a collection of information if it does not display a currently valid OMB control number. **PLEASE DO NOT RETURN YOUR FORM TO THE ABOVE ADDRESS.**

1. REPORT DATE *(DD–MM–YYYY)*	2. REPORT TYPE	3. DATES COVERED *(From — To)*
23–03–2017	Master's Thesis	Apr 2016 — Mar 2017

4. TITLE AND SUBTITLE

The Fresnel Zone Light Field Spectral Imager

5a. CONTRACT NUMBER

5b. GRANT NUMBER

5c. PROGRAM ELEMENT NUMBER

6. AUTHOR(S)

Hallada, Francis D., Major

5d. PROJECT NUMBER

5e. TASK NUMBER

5f. WORK UNIT NUMBER

7. PERFORMING ORGANIZATION NAME(S) AND ADDRESS(ES)

Air Force Institute of Technology
Graduate School of Engineering and Management (AFIT/EN)
2950 Hobson Way
WPAFB OH 45433-7765

8. PERFORMING ORGANIZATION REPORT NUMBER

AFIT-ENP-MS-17-M-095

9. SPONSORING / MONITORING AGENCY NAME(S) AND ADDRESS(ES)

Intentionally left blank

10. SPONSOR/MONITOR'S ACRONYM(S)

11. SPONSOR/MONITOR'S REPORT NUMBER(S)

12. DISTRIBUTION / AVAILABILITY STATEMENT

DISTRIBUTION STATEMENT A:
APPROVED FOR PUBLIC RELEASE; DISTRIBUTION UNLIMITED.

13. SUPPLEMENTARY NOTES

This work is declared a work of the U.S. Government and is not subject to copyright protection in the United States.

14. ABSTRACT

This thesis provides a computational model and the first experimental demonstration of a Fresnel zone light field spectral imaging (FZLFSI) system. This type of system couples an axial dispersion binary diffractive optic with light field (plenoptic) camera designs providing a snapshot spectral imaging capability. A computational model of the system was developed based on wave optics methods using Fresnel propagation. It was validated experimentally and provides excellent demonstration of system capabilities. The experimentally demonstrated system was able to synthetically refocus monochromatic images across greater than a 100nm bandwidth. Furthermore, the demonstrated system was modeled to have a full range of approximately 400 to 800nm with close to a 15nm spectral sampling interval. Experimental demonstration also showed the capability to resolve between and process two different spectral signatures from a single snapshot. For future FZLFSI designs, the study noted there is a fundamental design trade-off, where improved spectral and spatial resolution reduces the spectral range of the system.

15. SUBJECT TERMS

Fresnel zone plate, photon sieve, snapshot spectral imaging, light field camera, plenoptic

16. SECURITY CLASSIFICATION OF:			17. LIMITATION OF ABSTRACT	18. NUMBER OF PAGES	19a. NAME OF RESPONSIBLE PERSON
a. REPORT	b. ABSTRACT	c. THIS PAGE			Lt Col Anthony L. Franz, AFIT/ENP
U	U	U	UU	99	19b. TELEPHONE NUMBER *(include area code)* (937) 255-3636, x4429; anthony.franz@afit.edu